# An Investigation of Inter-Ligand Coordination and Flexibility: IRMPD Spectroscopic and Theoretical Evaluation of Calcium and Nickel Histidine Dimers

Brandon C. Stevenson,<sup>†</sup> Katrin Peckelsen,<sup>×</sup> Jonathan Martens,<sup>‡</sup> Giel Berden,<sup>‡</sup> Jos Oomens,<sup>‡,§</sup> Mathias Schäfer,<sup>×</sup> and P. B. Armentrout<sup>†,\*</sup>

<sup>†</sup>Department of Chemistry, University of Utah, 315 South 1400 East, Room 2020, Salt Lake City, Utah 84112, USA

<sup>‡</sup>Radboud University, Institute for Molecules and Materials, FELIX Laboratory, Toernooiveld 7, 6525 ED Nijmegen, The Netherlands

§van't Hoff Institute for Molecular Sciences, University of Amsterdam, Science Park 904, NL-1098 XH Amsterdam, The Netherlands

#### Abstract.

Metallated gas-phase structures consisting of an intact and deprotonated histidine (His) ligand,  $M(His-H)(His)^+$ , where M = Ca and Ni, were examined using infrared multiple photon dissociation (IRMPD) action spectroscopy utilizing light from a free-electron laser (FEL). In parallel, *ab initio* quantum-chemical calculations identified several low-energy isomers for each complex. Experimental action spectra were compared to linear absorption spectra calculated at the B3LYP level of theory, using the 6-311+G(d,p) basis set. Single-point energies were calculated at B3LYP, B3LYP-GD3BJ, B3P86, and MP2(full) levels using the 6-311+G(2d,2p) basis set. For  $Ca(His-H)(His)^+$ , the dominant structure has the metal center coordinating with the  $\pi$  nitrogen of the imidazole ring  $(N_\pi)$  and both oxygen atoms of the carboxylate group of the deprotonated His ligand while coordinating with the backbone amine  $(N_\alpha)$ ,  $N_\pi$ , and the carbonyl oxygen of the carboxylic acid of the intact His ligand. The  $Ni(His-H)(His)^+$  species coordinates the metal ion through  $N_\alpha$ ,  $N_\pi$ , and the carbonyl oxygen for both the deprotonated and intact His ligands, but also shows evidence for a minor secondary structure where the deprotonated His coordinates the metal

<sup>\*</sup> Department of Chemistry, University of Cologne, 50923 Cologne, Germany

<sup>\*</sup> Corresponding author, e-mail: armentrout@chem.utah.edu

at  $N_{\alpha}$ ,  $N_{\pi}$ , and the deprotonated carbonyl oxygen and the intact His ligand is zwitterionic, coordinating the metal with both carboxylate oxygens. Different levels of theory predict different ground structures, highlighting the need for utilizing multiple levels of theory to help identify the gas-phase structure actually observed experimentally.

**Keywords:** amino acid, density functional theory, infrared multiple photon dissociation action spectroscopy, metal ion coordination, NikA ATP-binding cassette transporter

#### Introduction

Transition metals play a vital role in protein structure and activity. Urease, a multimeric enzyme that contains 24 nickel ions per active complex, hydrolyzes urea to produce ammonia and bicarbonate,<sup>1</sup> which then act as buffers to allow bacteria to survive in acidic environments.<sup>2</sup> Successful bacterial colonization events must contend with the nanomolar concentrations of nickel in the human body.<sup>3</sup> *E. coli* expresses the NikABCDE ATP-binding cassette transporter, which does not bind the bare metal nickel ion, but instead binds a Ni(His)<sub>2</sub> complex, where the histidine (His) ligands are the L stereoisomer.<sup>4-7</sup> The process by which NikA, the Ni(II) binding component, imposes metal-specific recognition remains an open question. One possibility is that the metal's identity in the M(His)<sub>2</sub> complex induces conformational changes in the ligand itself, by which NikA can discriminate.

Fundamental interactions between metals and chelating amino acids have been widely studied using infrared multiple photon dissociation (IRMPD) action spectroscopy with complementary quantum chemical calculations. Here, we examine the nickel dication simultaneously complexed with a deprotonated histidine (His-H)<sup>-</sup> and a neutral histidine (His) ligand. The parallel calcium complex, Ca(His-H)(His)<sup>+</sup>, is also explored to probe the role of metal identity in the observed conformation. Calcium was chosen because its metal dication is much larger than the nickel dication (1.00 vs. 0.55 Å) and more polarizable. Recorded IR action spectra were compared to calculated spectra of low-lying conformations to identify the specific conformation for these complexes. Further comparisons are made to our recent studies of the

metallated dimers Zn(His-H)(His)<sup>+</sup> and Cd(His-H)(His)<sup>+</sup>, to determine the effects of the metal ion identity on the resulting structures.<sup>14</sup>

# **Experimental and Computational Section**

Mass Spectrometry and IRMPD Photodissociation

Collection of the infrared action spectra was performed at the Free Electron Laser for Infrared experiments (FELIX) laboratory at Radboud University in Nijmegen, the Netherlands. 15 Experimental infrared spectra were obtained using a modified quadrupole ion trap (QIT) mass spectrometer (Bruker, Amazon Speed ETD) that allows optical access by the free-electron laser (FEL).<sup>16</sup> Precursor reactant ions were formed by electrospray ionization (ESI) of a solution previously detailed in the literature.<sup>17</sup> In short, a metal salt/ethanol solution of either calcium chloride or nickel acetate was layered atop an aqueous solution of pyridine and L-histidine. The solution was kept at room temperature for one week, resulting in a purple solution in the case of the nickel solution and a clear, colorless solution in the case of the calcium. This solution was further diluted in methanol to sub-millimolar concentration for further analysis. The Ca(His-H)(His)<sup>+</sup> and Ni(His-H)(His)<sup>+</sup> ions were then mass isolated and irradiated with two IR laser pulses while monitoring the parent and fragment ions. The FEL operated at a 10 Hz macropulse repetition rate with an energy up to 100 mJ per pulse. IRMPD spectra were produced by plotting the integrated intensities of the precursor  $(I_P)$  and fragment  $(I_F)$  ion mass peaks as a function of the FEL laser frequency, where the photofragmentation yield is  $-\ln[\sum I_P/(\sum I_F + \sum I_P)]$ . <sup>18</sup> A linear correction was applied to the yield to account for variation in the IR laser pulse energy, which is suitable for this experiment because absorption is virtually linear until saturation occurs. 18-19

# Computational Details

Gaussian16 was used to identify low-energy conformers.<sup>20</sup> Preliminary conformer identification started with optimized structures found for the previously explored Zn(His-H)(His)<sup>+</sup> system.<sup>14</sup> The zinc metal center of those structures was replaced with either a calcium or nickel

metal ion. For the nickel-containing species, both triplet and singlet spin states were investigated. Initial optimizations done at the B3LYP/6-31G(d) level of theory using the "loose" keyword to facilitate convergence were subsequently geometry optimized at the B3LYP/6-311+G(d,p) level of theory. Unique structures found for either metal species were reoptimized after replacing the metal center with the alternative ion to ensure conformational coverage. Vibrational frequencies obtained from these optimized structures were scaled by 0.975 and broadened using a Gaussian line shape (25 cm<sup>-1</sup> FWHM) for comparison to IRMPD spectra.<sup>21</sup> This combination of theory and scaling factors is consistent with previous work for similar systems.<sup>14,22-29</sup>

The relative energetic spacing of these B3LYP/6-311+G(d,p) optimized geometries was determined by single-point energy (SPE) calculations at the B3LYP, B3P86, and MP2(full) levels of theory using the 6-311+G(2d,2p) basis set. Zero-point energy (ZPE) and thermal corrections were applied to SPEs to provide 0 K relative enthalpies and 298 K Gibbs energies, respectively. Vibrational frequencies were scaled by 0.989 when used to calculate ZPE and thermal corrections.<sup>30</sup>

To determine whether dispersion forces affected the calculated geometries and energies, the B3LYP/6-311+G(d,p) optimized structures were again optimized after adding the GD3BJ empirical dispersion method. For most of the species explored here, this optimization resulted in no perceptible changes to the structures. This level of theory was also used to calculate vibrational frequencies to provide 0 K relative enthalpies and 298 K Gibbs energies using the aforementioned scaling factor (0.989). The B3LYP-GD3BJ SPE was calculated using the larger 6-311+G(2d,2p) basis set.

#### **Results and Discussion**

#### Nomenclature

The nomenclature used to identify these metallated amino acid structures is consistent with previous literature and follows the strategy utilized in our most recent study to facilitate comparison.<sup>14</sup> Metal-binding sites ( $N_{\alpha}$  = amino nitrogen,  $N_{\pi}$  = imidazole "pros" nitrogen, CO =

carbonyl oxygen,  $CO_2^-$  = both oxygens of a carboxylate) are listed in square brackets, with the deprotonated histidine ligand coordination sites listed first and intact histidine ligand listed second. Zwitterionic structures are further indicated by a negative sign next to a hydrogen atom's original position and listing the protonated site in parentheses after the square brackets. If required to distinguish similar structures, the coordination label is followed by a description of the orientation of four dihedral angles using c (cis, 0–45°), g (gauche, 45–135°), and t (trans, 135–180°). The first letter describes the  $\angle$ OCCC dihedral angle of the (His-H)<sup>-</sup> ligand starting at the oxygen closest to the metal center. In the surveyed calcium species, when the gauche angle is negative, its sign (-) is specified when needed to discriminate from otherwise similar structures. The intact His ligand is described by the three subsequent letters, starting at the carboxylic acid hydrogen, which describe the  $\angle$ HOCC,  $\angle$ OCCC, and  $\angle$ CCCC dihedral angles.

For the Ni-containing species, both triplet and singlet spin species were explored as they were found to be competitive in relative energy. A superscript 1 is used to identify singlet species. For the Ca containing species, the large metal center allows pairs of isomers having identical metal binding sites and ligand dihedral angle designations but differing in the relative orientation of the ligands. To differentiate these isomers, they are simply noted with a number in parentheses, with the lowest energy structure being numbered first.

## Relative Energies and Structures of Ca Complexes

The energies of the nine lowest-lying calcium complex isomers can be found in Table 1, which includes both their single-point enthalpies at 0 K and 298 K Gibbs energies calculated at the B3LYP, B3LYP-GD3BJ, B3P86, and MP2 levels of theory relative to the lowest-energy conformer. Structures of select conformers are shown in Figure 1; additional structures can be found in the Supporting Information (Figure S1). All four levels of theory predict the hexadentate  $[N_{\pi},CO_2^-][N_{\alpha},N_{\pi},CO]g_-tgg(1)$  to be the ground structure (GS) at 298 K, and MP2 predicts this structure is the GS at 0 K as well. For this structure, the metal center coordinates with the (His-H)<sup>-</sup> ligand at the  $\pi$  nitrogen of the imidazole ring and both oxygen atoms of the deprotonated

carboxylate group with equal r(Ca-O) bond lengths of 2.321 Å. The intact His ligand coordinates the metal center by interactions with the backbone amine,  $\pi$  nitrogen of the imidazole ring, and the carbonyl oxygen of the carboxylic acid.

Two similar structures,  $[N_{\pi},CO_2^-][N_{\alpha},N_{\pi},CO]$ gtgg and  $[N_{\pi},CO_2^-][N_{\alpha},N_{\pi},CO]$ g\_tgg(2) were also found that exhibit very similar binding and coordination of the His ligands as the GS. In all three structures, the His ligand has the same geometry and coordination to Ca. The  $[N_{\pi},CO_2^-][N_{\alpha},N_{\pi},CO]$ gtgg structure differs from the GS in the relative positioning of the side-chain conformation of the (His-H)<sup>-</sup> ligand, which results in asymmetric metal-coordination bond distances with the (His-H)<sup>-</sup> carboxylate oxygens (2.299 and 2.345 Å, Table 2). In this structure and the GS, the  $CO_2^-$  oxygens lie opposite the CO oxygen. The  $[N_{\pi},CO_2^-][N_{\alpha},N_{\pi},CO]$ g\_tgg(2) conformer differs from the gtgg structure in that the (His-H)<sup>-</sup> imidazole ring is rotated relative to the His ligand, such that the three oxygens now occupy adjacent coordination sites. This change in relative ligand orientation results in slightly longer bond distances (0.01 – 0.05 Å, Table 2) for the  $N_{\alpha}$ ,  $N_{\pi}$ , and  $CO_2^-$  coordination sites when compared to the GS, with a relative decrease of 0.03 Å for the His ligand carbonyl oxygen. These two structures are predicted to be 3 – 6 kJ/mol and 9 – 15 kJ/mol higher in energy at 298 K than the GS, respectively.

The zwitterionic, pentadentate  $[N_{\alpha},N_{\pi},CO^{-}][CO_{2}^{-}](N_{\pi}H^{+})$  structure, Figure 1, is characterized by the intact His ligand diverging from the canonical histidine structure in that the carboxylic acid proton has been transferred to the  $\pi$  nitrogen. This zwitterionic His ligand allows strong metal binding to both oxygen atoms of the His carboxylate group while simultaneously stabilizing the entire complex through an inter-ligand  $CO^{\bullet}HN_{\pi}$  hydrogen bond. Regarding the (His-H)<sup>-</sup> ligand, the calcium ion coordinates with the backbone amine nitrogen,  $\pi$  nitrogen of the imidazole, and deprotonated carbonyl oxygen of the carboxylate. The three density functional theory (DFT) approaches, B3LYP, B3LYP-GD3BJ, and B3P86, predict this structure to be 0.3 – 1.3 kJ/mol higher in energy than the GS at 298 K and to be the GS at 0 K. The MP2 level of theory places this structure 13 kJ/mol higher than the GS. The similar  $[N_{\alpha},N_{\pi},CO^{-}][N_{\alpha},CO](N_{\pi}H^{+})$  structure was also located and is predicted to be 29 – 44 kJ/mol higher in energy than the GS. This

conformer is structurally similar to the aforementioned  $[N_{\alpha}, N_{\pi}, CO^{-}][CO_{2}^{-}](N_{\pi}H^{+})$ , maintains the  $CO \cdot HN_{\pi}$  hydrogen bond, but the calcium coordinates with the backbone amine and one oxygen of the carboxylate of the zwitterionic His ligand.

Two additional hexadentate structures were also located,  $[N_{\alpha},N_{\pi},CO^-][N_{\alpha},N_{\pi},CO](1)$  and  $[N_{\alpha},N_{\pi},CO^-][N_{\alpha},N_{\pi},CO](2)$ , and coordinate the metal center with the amine nitrogen,  $\pi$  nitrogen of the imidazole ring, and the oxygen of the carboxylic acid for both the deprotonated and intact His ligands. Even though both of these structures exhibit the highest number of coordination sites found, theory predicts these structures lie 5-13 kJ/mol and 12-21 kJ/mol above the hexadentate GS, respectively. As shown in Figure 1, these structures differ in the relative orientation of the histidine ligands, where the lower-energy structure has the imidazole rings pointing in opposite directions, and the higher-energy structure has them pointing in the same direction. The bond distances of the metal coordination sites of the (His-H)<sup>-</sup> ligand are relatively unaffected by the relative orientation of the ligands. For the His ligand, the Ca-O bond length is minimally perturbed by the different ligand orientation, whereas the Ca-N<sub>\alpha</sub> and Ca-N<sub>\pi</sub> bond lengths are inversely related, i.e., the higher-energy conformer has a longer Ca-N<sub>\alpha</sub> and shorter Ca-N<sub>\pi</sub> bond lengths relative to those of the lower-energy conformer. The observed energetic penalty of 7-8 kJ/mol for the relative positioning of the histidine ligands could reflect the energetic preference for the metal to coordinate with the backbone amine.

At 12-20 kJ/mol above the GS, another zwitterionic structure,  $[N_{\alpha},N_{\pi},CO^{-}][CO_{2}^{-}](N_{\alpha}H^{+})$ , was located, which has similar coordination to the aforementioned  $[N_{\alpha},N_{\pi},CO^{-}][CO_{2}^{-}](N_{\pi}H^{+})$  structure. Here, the carboxylic acid proton is attached to the backbone nitrogen, providing intraligand coordination with the  $\pi$  nitrogen of the imidazole ring. The protonated  $N_{\alpha}$  group withdraws electron density from the imidazole ring via this hydrogen bond, which allows for inter-ligand coordination between the  $N_{\tau}H$  and the non-bonding carbonyl oxygen of the (His-H)<sup>-</sup> ligand,  $CO^{\bullet}HN_{\tau}$ . At an even higher 37-56 kJ/mol above the GS, the  $[N_{\alpha},N_{\pi},CO^{-}][N_{\alpha},N_{\pi}]$  structure was found, where the calcium is no longer coordinating with either oxygen of the intact His ligand. In addition to the conformers presented in Table 1, twelve other structures were found, as listed in

Table S1 and shown in Figure S1, and lie 43-206 kJ/mol above the GS at 298 K. The majority of these structures were found by starting with singlet nickel geometries. Generally, they exhibit  $[N_{\alpha},CO^{-}][N_{\alpha},N_{\pi}]$  coordination with subtle changes in the amino acid backbone of the attached ligands.

Relative Energies and Structures of Ni Complexes

Table 3 displays the relative energies for the nine lowest-lying Ni(His-H)(His)<sup>+</sup> structures, with selected structures shown in Figure 2. MP2 predicts the  $[N_{\alpha},N_{\pi},CO^{-}][N_{\alpha},N_{\pi},CO]$  structure to be the GS, which is similar to calcium's  $[N_{\alpha},N_{\pi},CO^{-}][N_{\alpha},N_{\pi},CO](2)$  structure. Replacing the metal center with a nickel atom results in significantly shorter metal-coordination bond distances (by 0.17-0.49 Å) for all binding sites, Table 2, rationalized by the different metal ionic radii. B3LYP-GD3BJ places this structure less than one kJ/mol higher in energy than its predicted 298 K GS,  $[N_{\alpha},N_{\pi},CO^{-}][N_{\alpha},N_{\pi}]$ , whereas B3LYP and B3P86 place this structure 9 and 2 kJ/mol, respectively, at 298 K above their predicted GS,  $[N_{\alpha},N_{\pi},CO^{-}][CO_{2}^{-}](N_{\pi}H^{+})$ .

The B3LYP-GD3BJ GS,  $[N_{\alpha},N_{\pi},CO^-][N_{\alpha},N_{\pi}]$ , is predicted by the other three levels of theory to be 4 – 10 kJ/mol higher at 298 K. This structure was identified by taking the  $Ca^{2+}$   $[N_{\alpha},N_{\pi},CO^-][N_{\alpha},N_{\pi},CO](1)$  structure, where the His ligands are inverted relative to one another, and replacing the metal center with nickel having a triplet spin state. When optimized with a smaller basis set, 6-31G(d), the carbonyl oxygen of the carboxylic acid on the His ligand coordinates with the Ni center, and the overall structure mirrors that of the hexadentate calcium isomer, r(Ni-O) = 2.45 Å. Then, when optimizing with the larger 6-311+G(d,p) basis set, the carboxylic acid group swivels away from the metal center, r(Ni-O) = 3.30 Å. The B3LYP, B3P86, and MP2 SPE's were calculated using this structure. To test whether optimization methods affect the optimized structures, all structures were reoptimized at the B3LYP-GD3BJ/6-311+G(d,p) level to account for empirical dispersion effects. During this alternate optimization for this species, the carboxylic acid group swivels back towards the metal center, r(Ni-O) = 2.45 Å, Table 2. Therefore, including empirical dispersion interactions at the B3LYP-GD3BJ level lead to a GS that favors hexadentate coordination, whereas the B3LYP optimization yields pentadentate coordination as

the GS. Similar changes in coordination were not observed for the remaining species of either metal.

The B3LYP and B3P86 GS,  $[N_{\alpha},N_{\pi},CO^{-}][CO_{2}^{-}](N_{\pi}H^{+})$ , is qualitatively similar to that of the calcium species, with the significant difference being shorter coordination bond distances. B3LYP-GD3BJ and MP2 place this structure 9 and 27 kJ/mol above their GS, respectively. If the His coordination is altered to  $[N_{\alpha},N_{\pi},CO^{-}][N_{\alpha},CO^{-}](N_{\pi}H^{+})$ , the structure is slightly higher in energy, 10-14 kJ/mol for B3LYP and B3P86, but only 0.2 and 3.3 kJ/mol higher for B3LYP-GD3BJ and MP2, respectively. Likewise, moving the proton on the zwitterionic His ligand to  $N_{\alpha}$ ,  $[N_{\alpha},N_{\pi},CO^{-}][CO_{2}^{-}](N_{\alpha}H^{+})$ , raises the energy by 21-25 kJ/mol for B3LYP and B3P86, but by 17 and 10 kJ/mol for B3LYP-GD3BJ and MP2, respectively. The  $[N_{\pi},CO_{2}^{-}][N_{\alpha},N_{\pi},CO]$  structure was also located and is predicted to be 21-27 kJ/mol above the respective GSs.

Both triplet and singlet spins were investigated for the nickel-containing structures. Three of the lowest-lying singlet structures are listed in Table 3. The two lowest-energy conformers according to B3LYP and B3P86 present similar metal-ligand coordination, where the metal center coordinates with the backbone amine nitrogen of both histidine ligands, the carboxylate oxygen of the (His-H)<sup>-</sup> ligand, and the  $\pi$  nitrogen of the imidazole ring of the intact His ligand,  $[N_{\alpha},CO^-][N_{\alpha},N_{\pi}]^1$ . As can be seen in Figure 2 for the ttgt conformer, the nickel has a square-planar coordination, as is typically favored for low-spin  $Ni^{2+}$  (3d<sup>8</sup>) complexes. B3LYP-GD3BJ and MP2 theory predict that the  $[N_{\alpha},N_{\pi}][N_{\alpha},CO^-](N_{\pi}H^+)^1$  conformer lies lower than the  $[N_{\alpha},CO^-][N_{\alpha},N_{\pi}]^1$  conformers. Comparing the  $[N_{\alpha},N_{\pi},CO^-][N_{\alpha},CO^-](N_{\pi}H^+)$  and  $[N_{\alpha},N_{\pi}][N_{\alpha},CO^-](N_{\pi}H^+)^1$  structures, both structures exhibit the inter-ligand  $CO^{\bullet}HN_{\pi}$  coordination that stabilizes the overall complex discussed above. When the metal center has triplet spin, the carbonyl oxygen of the (His-H)<sup>-</sup> ligand coordinates to the metal center, Figure 2 (2.01 Å, Table 2). When the metal center is changed to singlet spin, the optimization moves this oxygen atom away from the metal center (3.07 Å, Table 2), providing the favored square-planar coordination while still maintaining the characteristic inter-ligand hydrogen bond for these  $N_{\pi}H^+$  structures.

Thirty additional structures were identified for Ni(His-H)(His)<sup>+</sup>; relative energies can be found in Table S2, and structures are shown in Figure S2. Although energetically competitive with some of the higher-energy triplet species, all singlet species explored here are predicted to be 16-236 kJ/mol above the GS. In general, all four levels of theory show the same general trend across these structures, with MP2 predicting the highest relative energies for the singlet spin species. The vast majority of the higher energy structures exhibit  $[N_{\alpha},CO^-][N_{\alpha},N_{\pi}]$  coordination with subtle changes in the dihedral angles of the amino acid backbone of both ligands.

## IRMPD Spectra of Metallated His Dimers

Infrared photodissociation spectra of both metallated species, Ca(His-H)(His)<sup>+</sup> (m/z 349) and Ni(His-H)(His) $^+$  (m/z 367), are shown in Figure 3. Several photodissociation pathways were observed for both species and correspond primarily to H<sub>2</sub>O, NH<sub>3</sub>, HCN, CO, or CO<sub>2</sub> losses. Supporting Information Table S3 contains a complete tabulation of product ions observed during the experiment. For the calcium complex, two products m/z 156 (H<sup>+</sup>His) and m/z 194 gave different dissociation spectra than all other fragments, as shown in Figure S3, which compares the normalized fragment intensities as a function of wavelength. The m/z 156 product, in particular, is characterized by extensive dissociation across much of the experimental wavelength range, with an aberrant band at 587 cm<sup>-1</sup>. The m/z 194 product shares several features with the other fragmentation products while also having a similar band as the m/z 156 product at 560 cm<sup>-1</sup>. Theoretical investigations could find no low energy form of Ca(His-H)(His)<sup>+</sup> that could dissociate readily to form (H<sup>+</sup>His). This observation coupled with the very different spectrum led us to conclude that this product comes from an unknown contaminant at m/z 349. The fragment found at m/z 194 is consistent with Ca(His-H)(His)<sup>+</sup> losing the intact His ligand, but because it also shows distinct fragmentation behavior at low wavenumbers when compared to the remaining fragment ions, we conclude that this fragment can be produced from the contaminant as well. One possibility for the isobaric contaminant is the potassiated histidine dimer, K(His)<sub>2</sub><sup>+</sup>, which could readily yield K<sup>+</sup>His at m/z 194 and plausibly form H<sup>+</sup>His at m/z 156. To avoid the contaminant contributing to the Ca(His-H)(His)<sup>+</sup> spectra, neither the m/z 156 or 194 fragments were used in the yield calculation.

No vibrational bands are observed below 1000 cm<sup>-1</sup> for either species, except for the very weak band at 586 cm<sup>-1</sup> in the Ni(His-H)(His)<sup>+</sup> spectrum. In this spectral range, the IR laser pulse energy is not enough to reach the dissociation threshold upon resonant vibrational excitation. A similar effect was observed for the analogous Zn and Cd histidine complexes.<sup>14</sup> For these two complexes, one third of the laser pulse energy was enough to record the spectrum in the 1000-1800 cm<sup>-1</sup> range, whereas full laser pulse energy was needed to observe bands below 1000 cm<sup>-1</sup>. For the nickel species, an additional IRMPD spectrum was also available from the Fourier transform ion cyclotron resonance mass spectrometer (FTICR-MS),<sup>33-35</sup> which operated at a much lower pressure than the QIT MS thereby reducing the effect of collisional cooling in the IRMPD process.<sup>16,36</sup> The resulting yield spectra are compared in Figure S4. There, the majority of the bands are present regardless of the instrument being used, with the marked exception of the band centered at 590 cm<sup>-1</sup>, which is more prominent in the FTICR-MS spectrum, along with minor bands between 650 – 1000 cm<sup>-1</sup>. For comparison to theoretical spectra, the IRMPD spectrum from the QIT instrument is used in the discussion below.

Significant features of the Ca(His-H)(His)<sup>+</sup> spectra are centered at 1724, 1530 (broad), 1435, 1167, and 1081 cm<sup>-1</sup>, with some more minor features found at 1325 and 587 cm<sup>-1</sup>. Several of these bands are present for the nickel species as well but are redshifted by 3 – 24 cm<sup>-1</sup>. Such shifts are consistent with nickel being heavier than calcium, with stronger binding for the smaller nickel dication, and with the transfer of electron density towards the metal center (away from the intramolecular ligand bonds). The experimental nickel band centered at 1709 cm<sup>-1</sup> is the most intense feature observed for this species and appears to have a shoulder at lower frequency in the QIT spectrum that is not present in the calcium spectrum. Notably, the FTICR-MS spectrum of this species also has a small peak at 1781 cm<sup>-1</sup> on the high frequency side of this band. The nickel spectrum has two smaller bands at 1565 and 1517 cm<sup>-1</sup> that replace the broad band at 1530 cm<sup>-1</sup> seen for calcium. Additional peaks centered at 1275 and 1045 cm<sup>-1</sup> appear in the nickel spectrum.

In sum, the spectra indicate some similarities as well as the presence of different binding modes for these two complexes that are explored further below.

Comparison of Experimental and Theoretical Spectra: Ca(His-H)(His)<sup>+</sup>

A comparison of the experimental spectrum for the calcium complex with six calculated spectra is shown in Figure 4. A list of the calculated frequencies and intensities can be found in Table S4. The GS determined by all four levels of theory,  $[N_{\pi}, CO_2^-][N_{\alpha}, N_{\pi}, CO]g.tgg(1)$ , replicates most of the major features of the experimental spectra. In detail, bands are predicted at 1713 (coordinated CO stretch of His); 1512 (coordinated CO asymmetric stretch of (His-H) with minor contributions from backbone CH motion and N<sub>α</sub>H<sub>2</sub> twist); 1434, 1415 (N<sub>τ</sub>H in-plane bend and coordinated CO symmetric stretch of (His-H) ligand); 1400 (COH bend); 1170, 1156 (COH bend and stretch with contributions from the N<sub>α</sub>H<sub>2</sub> twist of the His ligand); and 1069 (CN<sub>τ</sub>C imidazole and CH backbone stretch of His ligand). This structure predicts two bands at 1631 and 1622 cm<sup>-1</sup>, which correspond to the N<sub>α</sub>H<sub>2</sub> scissor motion of the (His-H)<sup>-</sup> and His ligands, respectively. In previous studies of metallated amino acids, 14,19,22-25,28,37-41 this scissor motion is typically redshifted by 22 - 42 cm<sup>-1</sup> because the motion is strongly anharmonic. Such a shift in this theoretical band would reproduce the higher wavenumber shoulder of the broad feature centered at 1530 cm<sup>-1</sup>. The theoretical bands located at 1325 and 1301 cm<sup>-1</sup> ( $N_{\alpha}H_2$  twist and COH bend with minor CH backbone and imidazole motion) reproduce the minor experimental bands centered at 1325 and 1310 cm<sup>-1</sup> well. Several theoretically predicted bands below 1000 cm<sup>-1</sup> are not observed in the experimental spectrum, which could result from the lower photon energy in this wavelength range preventing the ions from reaching the dissociation threshold, a phenomenon also observed for the analogous Zn and Cd metallated systems.<sup>14</sup>

The main discrepancy between the predicted and experimental spectra lies with the relative intensity of the bands. A direct comparison of the intensity of the two spectra needs to be done carefully because the theoretical spectra intrinsically assume a single-photon absorption process, whereas IRMPD requires the absorption of multiple photons to induce dissociation. Experimentally, the three major bands above 1400 cm<sup>-1</sup> decrease in intensity as the frequency

increases, and the theoretically derived bands do the opposite. This intensity discrepancy has been observed before on a very similar species, Ca(HisHis-H)<sup>+</sup>, and could be attributed to reduced laser power in this wavelength range, non-linear power dependence, anharmonic effects, or some combination thereof.<sup>8</sup>

To ascertain the effects of anharmonicity, additional frequency calculations were performed on the optimized  $[N_{\pi},CO_2^-][N_{\alpha},N_{\pi},CO]g.tgg(1)$  structure at the B3LYP/6-311+G(d,p) level using the keyword "freq=anharmonic". Figure 5 compares the results of these anharmonic calculations with the experimental IRMPD data. Here, the calculated anharmonic frequencies were scaled and were convoluted using a 25 cm<sup>-1</sup> Gaussian line  $[N_{\pi},CO_2^{-1}][N_{\alpha},N_{\pi},CO]g$ -tgg(1) anharmonic spectrum predicts a fundamental band at 1723 cm<sup>-1</sup> and a combination band at 1715 cm<sup>-1</sup> arising from the coordinated CO stretching of the His ligand and coupled N<sub>T</sub>H bending with His backbone motions, respectively, which nicely recreates the experimental feature observed there. The intensity of the fundamental band is 62% of its harmonic predicted intensity, better matching the observed spectrum. Now, the predicted anharmonic spectrum is dominated by the bands slightly above 1500 cm<sup>-1</sup>. The most intense band at 1518 cm<sup>-1</sup> <sup>1</sup> is the fundamental band matching the 1512 cm<sup>-1</sup> motion described above and has an intensity of 741 km/mol vs. 292 km/mol in the harmonic spectrum. Combination bands at 1505, 1518, 1519 cm<sup>-1</sup> (from various (His-H)<sup>-</sup> motions) and an overtone band at 1522 cm<sup>-1</sup> (from (His-H)<sup>-</sup> imidazole out-of-plane bend) also contribute to the peak that is the dominant feature in this predicted spectrum. The intensity of the experimental feature at 1435 cm<sup>-1</sup> is not predicted well here, but its position is matched by the two fundamental bands at 1438 cm<sup>-1</sup> (N<sub>7</sub>H bending of the (His-H)<sup>-</sup> ligand). Notably, the anharmonic spectrum no longer predicts much intensity below 1000 cm<sup>-1</sup>, in better agreement with the observed spectrum. Overall, the anharmonic  $[N_{\pi},CO_2^-][N_{\alpha},N_{\pi},CO]g$ tgg(1) spectrum recreates the experimental spectrum very well, increasing confidence that this structure is the dominant species present. Further, the relative positions of these bands compared to the experimental spectrum support the use of the 0.975 scaling factor for the harmonic calculations to account for anharmonic effects.

Figure 4 also compares the experimentally obtained spectrum to that predicted for the very low-lying  $[N_{\alpha},N_{\pi},CO^{-}][CO_{2}^{-}](N_{\pi}H^{+})$  structure. Here, neither of the predicted bands associated with  $N_{\pi}$  motion, 1671 (coordinated CO asymmetric stretch of (His-H)<sup>-</sup> with contributions from  $N_{\pi}H$  stretch and imidazole motion) or 1622 cm<sup>-1</sup> ( $N_{\pi}H$  wag) are readily apparent in the experimental spectrum. The band at 1607 cm<sup>-1</sup> ( $N_{\alpha}H_2$  scissor motion of (His-H)<sup>-</sup>) could be shifted because of anharmonic effects discussed above, and the intense band predicted at 1528 cm<sup>-1</sup> (coordinated CO asymmetric stretch with minor contributions from  $N_{\alpha}H_2$  twist and  $N_{\pi}H$  stretch of the His ligand) recreates some of the broad experimental band at 1530 cm<sup>-1</sup>. The predicted band at 1409 cm<sup>-1</sup> is slightly redshifted compared to the experimental band, but there is no experimental evidence for the intense band predicted at 1294 cm<sup>-1</sup> (coordinated CO stretch of the (His-H)<sup>-</sup> ligand with  $N_{\pi}H$  wag). Figure 5 shows the anharmonic vibrational calculation for this species. Although the experimental band at 1530 cm<sup>-1</sup> is reproduced well in this spectrum, none of the other features in this spectrum match those of experiment, with intense bands now present below 1000 cm<sup>-1</sup>. Thus, we conclude that this structure is not significantly populated, in agreement with the relative energy predicted at the MP2 level, but not by the DFT calculations. Using the calculated relative energies for the  $[N_{\pi},CO_2^-][N_{\alpha},N_{\pi},CO]g_{-}tgg(1)$  and  $[N_{\alpha},N_{\pi},CO^-][CO_2^-](N_{\pi}H^+)$  structures, an equilibrium distribution at 298 K using the B3LYP and B3P86 levels predicts a conformeric mixture of 54% and 47%, respectively. B3LYP-GD3BJ predicts 63% and 37%, whereas MP2 predicts >99% of the  $[N_{\pi},CO_2^-][N_{\alpha},N_{\pi},CO]g_{\tau}tgg(1)$  species being present.

Figure 4 also compares the experimental spectrum with computed spectra for both hexadentate  $[N_{\alpha},N_{\pi},CO^-][N_{\alpha},N_{\pi},CO]$  structures, as well as those of the zwitterionic  $[N_{\alpha},N_{\pi},CO^-][CO_2^-](N_{\alpha}H^+)$  and  $[N_{\alpha},N_{\pi},CO^-][N_{\alpha},CO](N_{\pi}H^+)$  species. Even though the ligands have adopted very different orientations relative to one another in the two hexadentate structures, their spectra are only subtly affected, with most of the difference between these two systems found in minor perturbations of low-frequency bands. Both of these species predict two intense bands above 1700 cm<sup>-1</sup>, which correspond to the coordinated CO stretch of both ligands, where the higher frequency band correlates to the His ligand. The higher energy band could be argued to recreate

the experimental feature at 1724 cm<sup>-1</sup>, but there is no meaningful evidence for the second band nor do these spectra reproduce the experimental bands at 1530 and 1435 cm<sup>-1</sup>. The  $[N_{\alpha},N_{\pi},CO^{-}][CO_{2}^{-}](N_{\alpha}H^{+})$  structure predicts four bands between 1600 and 1650 cm<sup>-1</sup>, whereas the  $[N_{\alpha},N_{\pi},CO^{-}][N_{\alpha},CO](N_{\pi}H^{+})$  structure predicts three intense bands slightly below 1700 cm<sup>-1</sup>. None of these predicted bands are present in the experimental spectrum. Finally, the relative energies of these species, 5-13, 12-21, 12-20, and 29-44 kJ/mol above the GS, suggest that none of these conformers is significantly populated in this experiment.

Comparison of Experimental and Theoretical Spectra Ni(His-H)(His)<sup>+</sup>

The photodissociation spectrum of Ni(His-H)(His)<sup>+</sup> is compared to theoretical spectra of low-lying structures in Figure 6. The hexadentate  $[N_{\alpha},N_{\pi},CO^-][N_{\alpha},N_{\pi},CO]$ , the MP2 GS, is able to recreate the intense experimental band passably by a predicted band at 1710 cm<sup>-1</sup> (uncoordinated asymmetric CO stretch of the (His-H)<sup>-</sup> ligand), but has a predicted band at higher wavenumber, 1731 cm<sup>-1</sup> (coordinated CO stretch and COH bend with minor  $N_{\alpha}H_2$  scissoring from the His ligand), rather than to the red of the main band. Bands predicted at 1605 and 1625 cm<sup>-1</sup> ( $N_{\alpha}H_2$  scissor motions of both ligands) would reproduce the experimental band at 1565 cm<sup>-1</sup> if redshifted because of the strong anharmonicity of these motions. The moderately intense bands predicted at 1330 cm<sup>-1</sup> ( $N_{\alpha}H_2$  wag and CH backbone motions of (His-H)<sup>-</sup> ligand) and 1285 cm<sup>-1</sup> (CO symmetric stretch and backbone motions of (His-H)<sup>-</sup> ligand) recreate the pair of peaks observed from 1250 – 1350 cm<sup>-1</sup>. Predicted bands at 1178 and 1145 cm<sup>-1</sup> ( $N_{\alpha}H_2$  twist and COH bend of the His ligand) could explain the band observed at 1144 cm<sup>-1</sup>. Finally, the doublet feature observed between 1000 – 1100 cm<sup>-1</sup> is predicted by the slightly redshifted bands at 1054 and 1020 cm<sup>-1</sup> ( $N_{\alpha}H_2$  wags of both ligands). In contrast to the calcium GS, this calculated harmonic spectrum does an excellent job of reproducing the observed band intensities.

 $[N_{\alpha},N_{\pi},CO^{-}][N_{\alpha},N_{\pi}]$ , the B3LYP-GD3BJ GS, also has a strong band at 1711 cm<sup>-1</sup> (coordinated CO stretch of (His-H)<sup>-</sup>), but the uncoordinated CO stretch of the His ligand shifts the highest frequency band to 1755 cm<sup>-1</sup>, far away from the experimentally observed shoulder. This structure reproduces the experimental bands between 1425 - 1100 cm<sup>-1</sup> reasonably well, but

predicts only a single band where a dual band near  $1050 \text{ cm}^{-1}$  is observed. These two discrepancies suggest that contributions from this species to the experimental spectrum are minimal, if present at all.  $[N_{\alpha},N_{\pi},CO^{-}][CO_{2}^{-}](N_{\pi}H^{+})$ , the B3LYP and B3P86 GS, recreates the high frequency carbonyl stretch but again does not reproduce the dual feature near  $1050 \text{ cm}^{-1}$ . The structure also predicts two bands centered at 1613 and  $1517 \text{ cm}^{-1}$ . The first band corresponds to vibrations from the  $N_{\alpha}H_{2}$  scissoring from both ligands and  $N_{\pi}H$  bending and imidazole motions. If redshifted by  $\sim 50 \text{ cm}^{-1}$ , as observed previously and discussed above, this band would nicely explain the experimental band observed at  $1565 \text{ cm}^{-1}$ . The second band arises from the coordinated, asymmetric stretch of the CO and imidazole motions of the His ligand and is the only structure of the three GS's to predict the minor experimental band centered at  $1518 \text{ cm}^{-1}$ . This observation suggests that this structure might be populated as a minor contributor.

A comparison between these three GS structures and their calculated anharmonic spectra is shown in Figure S5. The  $[N_{\alpha}, N_{\pi}, CO^{-}][N_{\alpha}, N_{\pi}, CO]$  spectrum does an acceptable job of recreating the highest frequency experimental band, predicting the band to be slightly blueshifted by 10 cm<sup>-1</sup>. The  $[N_{\alpha}, N_{\pi}, CO^{-}][N_{\alpha}, N_{\pi}]$  structure still yields a series of bands around 1751 cm<sup>-1</sup> that are not present in the experimental spectrum. The spectrum for the zwitterionic  $[N_{\alpha}, N_{\pi}, CO^{-}][CO_{2}^{-}](N_{\pi}H^{+})$  species recreates the experimental band at 1707 cm<sup>-1</sup> with good fidelity as well as some of the lower frequency bands, but notably predicts bands between 1596 – 1624 and 1347 –1380 cm<sup>-1</sup> for which there is scant experimental evidence and the bands near 1510 cm<sup>-1</sup> remain much larger than the small band observed experimentally. The anharmonic calculations therefore do not alter the conclusions reached above on the basis of the harmonic results shown in Figure 6.

The calculated equilibrium distribution of conformers at 298 K indicates that at the B3LYP level of theory,  $[N_{\alpha}, N_{\pi}, CO^-][N_{\alpha}, N_{\pi}, CO^-][N_{\alpha}, N_{\pi}, CO^-][N_{\alpha}, N_{\pi}]$  structures are predicted to make up ~3% of the conformer population each, with the  $[N_{\alpha}, N_{\pi}, CO^-][CO_2^-](N_{\pi}H^+)$  conformer making up the remaining 94%. For the same structures, B3LYP-GD3BJ predicts the distribution is 44%, 54%, and 2%, whereas B3P86 predicts 25%, 11%, and 64%. MP2 predicts the

 $[N_{\alpha},N_{\pi},CO^{-}][N_{\alpha},N_{\pi},CO]$  structure dominating the population at 98%, with <2% contribution from  $[N_{\alpha},N_{\pi},CO^{-}][N_{\alpha},N_{\pi}]$ , and <1% from the  $[N_{\alpha},N_{\pi},CO^{-}][CO_{2}^{-}](N_{\pi}H^{+})$ . On the basis of the experimental spectrum, the MP2 level of theory best describes the species comprising the majority of the spectrum but does not predict any appreciable contributions from the zwitterionic structure that may be present.

The Ni(His-H)(His)<sup>+</sup> IRMPD spectrum is also compared to three other conformations for completeness in Figure 6. The zwitterionic  $[N_{\alpha},N_{\pi},CO^{-}][N_{\alpha},CO^{-}](N_{\pi}H^{+})$  recreates several experimental features, and the two bands at 1085 and 1049 cm<sup>-1</sup> might recreate the experimental doublet, but does not explain the minor band at 1518 cm<sup>-1</sup> as well as the lower-lying  $[N_{\alpha},N_{\pi},CO^{-}][CO_{2}^{-}](N_{\pi}H^{+})$ . The  $[N_{\pi},CO_{2}^{-}][N_{\alpha},N_{\pi},CO]$ , the identified GS conformation for the calcium system, does not recreate the observed bands with the fidelity of the MP2 and B3LYP/B3P86 GS, as well as sitting 21 – 27 kJ/mol higher in energy than either of those structures. The lowest lying singlet conformation,  $[N_{\alpha},CO^{-}][N_{\alpha},N_{\pi}]$ ttgt<sup>1</sup>, predicts two intense carbonyl stretching bands at 1768 and 1739 cm<sup>-1</sup>, for which there is no experimental evidence. This comparison indicates that the observed species most likely has triplet spin, which is consistent with the previous characterization of the Ni(HisHis-H)<sup>+</sup> complex.<sup>8</sup>

Figure S6 presents a comparison of the Ni(His-H)(His)<sup>+</sup> IRMPD spectrum collected on the FTICR-MS instrument with the theoretical spectra. Similar to the QIT spectrum, the FTICR experimental spectrum is mostly consistent with the predicted spectrum for the  $[N_{\alpha},N_{\pi},CO^{-}][N_{\alpha},N_{\pi},CO]$  structure. The minute band at 586 cm<sup>-1</sup> previously observed in the QIT spectrum is now much more pronounced but is not predicted by this MP2 GS spectrum. This structure does predict a pair of peaks just above (624 cm<sup>-1</sup>,  $N_{\tau}$  out of plane bending and  $N_{\alpha}H_{2}$  twisting) and just below (575 and 565 cm<sup>-1</sup>,  $N_{\tau}$  out of plane bending of the His and (His-H)<sup>-</sup>, respectively) this wavenumber. The spectrum for the  $[N_{\alpha},N_{\pi},CO^{-}][N_{\alpha},N_{\pi}]$  structure does include a band at 602 cm<sup>-1</sup> (similar motion as the 624 cm<sup>-1</sup> band) and at 1755 cm<sup>-1</sup> (uncoordinated CO stretch of the His ligand), which could correspond to the high-frequency shoulder observed in the FTICR spectrum at 1781 cm<sup>-1</sup>; however, the latter could be an artifact whose magnitude has been amplified

by the power correction. These observations confirm the dominant conformer assignment provided above for the QIT IRMPD spectrum, but offer some indication for an additional conformer present in small amounts.

## Comparison to Similar Metallated Systems

IRMPD experiments on  $Zn(His-H)(His)^+$  and  $Cd(His-H)(His)^+$  have been previously reported. <sup>14</sup> The expansion here to the comparable complexes of Ni and Ca presents an opportunity to examine the conformational and energetic preferences of this dimeric histidine system with respect to metal identity. In this previous study, good agreement between the theoretical spectrum of the zwitterionic  $[N_{\alpha},N_{\pi},CO^-][CO_2^-](N_{\pi}H^+)$  structure and the experimental zinc spectrum was found, with a small contribution from  $[N_{\alpha},N_{\pi},CO^-][N_{\alpha},N_{\pi}]$  gtgg possible. For the Cd species, the dominant species was also identified as the  $[N_{\alpha},N_{\pi},CO^-][CO_2^-](N_{\pi}H^+)$  conformer, with trace contribution from  $[N_{\alpha},N_{\pi},CO^-][N_{\alpha},N_{\pi}]$  gtgg and/or  $[N_{\alpha},N_{\pi},CO^-][N_{\alpha},N_{\pi},CO]$  species. In the present work, the Ca and Ni metallated systems both exhibit a canonical conformer as the most dominant species present, with contributions from the zwitterionic  $[N_{\alpha},N_{\pi},CO^-][CO_2^-](N_{\pi}H^+)$  conformer possible for the Ni species.

Note that all three transition metal systems prefer coordination of the deprotonated His ligand in the  $[N_{\alpha},N_{\pi},CO^-]$  configuration. Ni<sup>2+</sup> (ionic radius = 0.55 Å)<sup>13</sup> then binds the His ligand in the similar  $[N_{\alpha},N_{\pi},CO]$  binding configuration, whereas  $Zn^{2+}$  (0.60 Å) and  $Cd^{2+}$  (0.78 Å)<sup>13</sup> prefer the zwitterionic  $[CO_2^-](N_{\pi}H^+)$  coordination stabilized by the  $CO^{\bullet}HN_{\pi}$  inter-ligand hydrogen bond. Given the similar sizes of Ni<sup>2+</sup> and  $Zn^{2+}$ , this change is likely dominated by differences induced by the 3d orbital populations (3d<sup>8</sup> and 3d<sup>10</sup>, respectively). In contrast, the larger  $Ca^{2+}$  (1.00 Å)<sup>13</sup> prefers the  $[N_{\pi},CO_2^-]$  coordination of the (His-H)<sup>-</sup> ligand accompanied by the canonical tridentate  $[N_{\alpha},N_{\pi},CO]$  coordination for His. This difference appears to be driven by steric effects. The bond lengths in Table 2 for the  $[N_{\pi},CO_2^-][N_{\alpha},N_{\pi},CO]$  conformers show that the M-N bond lengths for both ligands are 0.4 – 0.5 Å longer in the Ca GS than those for the Ni complex. The M-O bonds, in contrast, shorten by only 0.16-0.26 Å, suggesting that they cannot bind as tightly as they might otherwise because of inter-ligand interactions.

Energetically, a single theoretical method fails to predict the observed species for these four metallated complexes. For these metallated systems, MP2 reliably predicts an energetic penalty for the zwitterionic  $[N_{\alpha}, N_{\pi}, CO^{-}][CO_{2}^{-}](N_{\pi}H^{+})$  structure. In the case of Zn and Cd, this energetic penalty disagrees with experimental observations that clearly show this structure is the dominant species present, in agreement with predictions of B3LYP and B3P86 methods (B3LYP-GD3BJ identified the same GS as the MP2 level for the Cd system). For the Ni case, a similar B3LYP and B3P86 where the levels predict the zwitterionic trend emerges,  $[N_{\alpha},N_{\pi},CO^{-}][CO_{2}^{-}](N_{\pi}H^{+})$  structure as the GS. At the MP2 level, the Ni zwitterionic structure was predicted to have a more significant energetic penalty than the Zn and Cd systems (27 versus 5 – 10 kJ/mol, respectively), and instead predicts the canonical  $[N_{\alpha},N_{\pi},CO^{-}][N_{\alpha},N_{\pi},CO]$  structure as the GS. The MP2 GS prediction agrees better with the dominant features seen in the present experiment, but these relative energetics predict almost no contributions from the canonical hexadentate structure, for which there is minor experimental evidence. The B3LYP-GD3BJ level assigned the canonical  $[N_{\alpha}, N_{\pi}, CO^{-}][N_{\alpha}, N_{\pi}]$  structure to be the lowest-lying, slightly disfavoring hexadentate coordination by 0.5 kJ/mol.

Regarding the Ca system, all levels of theory indicate a clear preference for the  $[N_{\pi},CO_2^-][N_{\alpha},N_{\pi},CO]$ g.tgg(1) structure when the relative energies are corrected to 298 K Gibbs energies. (Notably, DFT levels would not predict the correct observed structure if 0 K values are used instead. Rather, they indicate the  $[N_{\alpha},N_{\pi},CO^-][CO_2^-](N_{\pi}H^+)$  structure is lowest in energy, Table 1.) At 298 K, the DFT levels of theory predict the zwitterionic structure to be <1.3 kJ/mol higher in energy, but the dearth of experimental evidence for such a structure suggests that these relative energetics are not accurate. MP2, with its 13 kJ/mol penalty to the zwitterionic structure, is more consistent with the experimental results. Overall, the ability of the MP2 level of theory to predict the conformation observed in the gas phase appears to be complicated when the possibility of zwitterionic species is present, because it places such a large energetic penalty on these structures. These results reiterate the need to consider multiple levels of theory as well as thermal corrections in order to increase the robustness of a theoretical survey of metallated structures.

Early work by Fraser and Harding determined the crystal structure of Ni<sup>2+</sup> complexed with two histidine ligands using 3D x-ray diffraction.<sup>42</sup> There, the complex adopted a hexadentate structure similar to the  $[N_{\alpha},N_{\pi},CO^{-}][N_{\alpha},N_{\pi},CO]$  MP2 GS species reported here, where the metal was complexed to each of the available binding sites of the histidine ligands. The noteworthy difference is that this assigned structure places the ligand's imidazoles 180° apart from one another. Using the theoretical techniques described herein, such a structure collapses to  $[N_{\alpha},N_{\pi},CO^{-}][N_{\alpha},N_{\pi}]$ . Even if such a structure were located, the calcium spectral comparison of  $[N_{\alpha},N_{\pi},CO^{-}][N_{\alpha},N_{\pi},CO](1)$  and (2) in Figure 4 shows that the relative orientation of the ligands results in only minor perturbations of less intense IR bands, such that the relative orientation of the His ligands is challenging to ascertain using IR spectroscopy.

Recent work on the crystal structure of Ni(His)<sub>2</sub> complexed with NikA suggests that the imidazole rings might be oriented in the same relative direction, as shown in the nickel  $[N_{\alpha},N_{\pi},CO^{-}]$   $[N_{\alpha},N_{\pi},CO]$  structure, Figure 2, but additional  $\pi$ -stacking effects associated with the NikA binding may also help direct this orientation.<sup>5</sup> With these additional effects in mind, it is still noteworthy that the identification of the biomimetic complex Ni(His-H)(His)<sup>+</sup> presented herein is consistent with the structural identification of the bound Ni(His)<sub>2</sub> ligand. In both cases, the Ni atom is in the same charge state. Ni(His-H)(His)<sup>+</sup> is the only complex, of the four divalent metals studied thus far, where the majority of the ion population adopts  $[N_{\alpha},N_{\pi},CO^{-}][N_{\alpha},N_{\pi},CO]$  coordination. Logically, it would follow that the metal-binding site of NikA is sensitive to coordination changes in the His ligands. This would suggest that extending the study of this histidine dimer complex to other transition metals could further elucidate the variance in the coordination and further the understanding of the NikA metal-selectivity mechanism.

#### Comparison to Predicted Energetics in Solution

A reviewer wonders whether the energetic ordering of the conformers is affected if a solvent continuum model is used. Using the keyword "SCRF=(solvent=water)", the five-lowest lying conformers for the Ni and Ca species were reoptimized and single-point energies were recalculated using the same levels of theory detailed above. The reoptimization did not

substantially affect these structures; however, their relative SPE's were affected and are detailed in Table S6. For the Ca containing structures, all four levels of theory identify  $[N_{\alpha},N_{\pi},CO^-][CO_2^-](N_{\pi}H^+)$  as the solvated GS at both 0 and 298 K. This prediction is consistent with the *in vacuo* SPE's performed at 0 K (except MP2), which also identified this conformation as the lowest in energy, Table 1. The solvated conformation next highest in energy is  $[N_{\alpha},N_{\pi},CO^-][N_{\alpha},N_{\pi},CO]$  at 13-23 kJ/mol, an increase of ~8 kJ/mol from its calculated *in vacuo* energetics. Notably,  $[N_{\pi},CO_2^-][N_{\alpha},N_{\pi},CO]$ g-tgg(1), the *in vacuo* GS at 298 K, is now predicted to be 31-41 kJ/mol higher than the GS. The two remaining conformations,  $[N_{\pi},CO_2^-][N_{\alpha},N_{\pi},CO]$ gtgg and  $[N_{\pi},CO_2^-][N_{\alpha},N_{\pi},CO]$ g-tgg(2), are predicted to be 31-42 kJ/mol and 35-47 kJ/mol above the solvated GS, increases of 29-35 and 26-32 kJ/mol, respectively. Clearly, the surrounding solvent stabilizes the zwitterionic  $[N_{\alpha},N_{\pi},CO^-][CO_2^-](N_{\pi}H^+)$  structure, thereby placing a substantial energetic penalty on the canonical structures. According to these energetics, a Boltzmann distribution would indicate that >99% of the ion population in solution would be present as  $[N_{\alpha},N_{\pi},CO^-][CO_2^-](N_{\pi}H^+)$ . As discussed above, analysis of the IRMPD spectrum for the Ca species indicates that there is none of this species present in the gas phase.

For the Ni complexes, different levels of theory continue to identify different GS's in implicit solvent. The MP2 GS continues to be  $[N_{\alpha},N_{\pi},CO^-][N_{\alpha},N_{\pi},CO]$  at both 0 and 298 K. B3LYP now identifies  $[N_{\alpha},N_{\pi},CO^-][N_{\alpha},CO^-](N_{\pi}H^+)$  as the GS at both 0 and 298 K. Interestingly, the B3P86 level predicts these structures to be nearly isoenergetic at 298 K, with  $[N_{\alpha},N_{\pi},CO^-][N_{\alpha},CO^-](N_{\pi}H^+)$  being lower in energy by less than a tenth of a kJ/mol, but assigns a 2 kJ/mol energetic penalty at 0 K. In solvent, the  $[N_{\alpha},N_{\pi},CO^-][N_{\alpha},N_{\pi}]$  structure does not converge to  $[N_{\alpha},N_{\pi},CO^-][N_{\alpha},N_{\pi},CO]$ , as previously observed in the B3LYP-GD3BJ *in vacuo* optimization, and this level of theory instead identifies  $[N_{\alpha},N_{\pi},CO^-][N_{\alpha},N_{\pi},CO]$  as the GS, consistent with the MP2 prediction. An equilibrium distribution of conformers at 298 K indicates that at the MP2 level, the  $[N_{\alpha},N_{\pi},CO^-][N_{\alpha},N_{\pi},CO]$  makes up 99% of the conformer population, with the remaining 1% coming from the  $[N_{\alpha},N_{\pi},CO^-][N_{\alpha},N_{\pi}]$  species. At the B3LYP level, the  $[N_{\alpha},N_{\pi},CO^-][N_{\alpha},N_{\pi},CO]$ ,  $[N_{\alpha},N_{\pi},CO^-][N_{\alpha},N_{\pi}]$ , and  $[N_{\alpha},N_{\pi},CO^-][N_{\alpha},CO^-](N_{\pi}H^+)$  make up 6, 11, and 83%, respectively. The

same species are expected to make up 42, 12, and 44% at the B3P86 level. The B3LYP-GD3BJ predicts the population to be composed of 63%  $[N_{\alpha},N_{\pi},CO^{-}][N_{\alpha},N_{\pi},CO]$ , 36%  $[N_{\alpha},N_{\pi},CO^{-}][N_{\alpha},N_{\pi}]$ , and <1%  $[N_{\alpha},N_{\pi},CO^{-}][CO_{2}^{-}](N_{\pi}H^{+})$ . Unlike in the Ca case, the X-ray crystallography of the Ni(His)<sub>2</sub> species is available, and as discussed above, indicates that the complex adopts a  $[N_{\alpha},N_{\pi},CO^{-}][N_{\alpha},N_{\pi},CO]$  coordination, where the imidazole moieties point 180° apart. This is inconsistent with the solvated B3LYP and B3P86 GS's described above and agrees best with the MP2 GS prediction, as also concluded for the *in vacuo* results.

For both calcium and nickel complexes, the inclusion of the solvent continuum model affects the energetic ordering but does not affect our original assignments of the metallated histidine dimers presented herein. In the future, identifying the gas-phase structures of Ca(His)<sub>2</sub><sup>+</sup> and Ni(His)<sub>2</sub><sup>+</sup> could be used to verify whether the biomimetic structures used herein are an accurate representation of solution-phase species.

### **Conclusions**

The IRMPD action spectra of Ca(His-H)(His)<sup>+</sup> and Ni(His-H)(His)<sup>+</sup> from 550 to 1810 cm<sup>-1</sup> are presented. A comparison of these spectra to theoretical linear absorption IR spectra calculated at the B3LYP/6-311+G(d,p) level finds good agreement between the 298 K GS conformers and the experimental spectra. For the calcium species, the  $[N_{\pi},CO_2^-][N_{\alpha},N_{\pi},CO]g_tgg(1)$  structure provides good agreement with the experiment, especially when employing anharmonic frequency calculations for this species, Figure 5. Missing bands preclude the presence of the zwitterionic  $[N_{\alpha},N_{\pi},CO^-][CO_2^-](N_{\pi}H^+)$  structure, confirmed by both the harmonic and anharmonic analysis. Here, the observations are consistent with the relative energetics predicted at the MP2 level, but not for DFT approaches, which appear to overly stabilize the zwitterionic species, as has been observed previously. For the Ni(His-H)(His)<sup>+</sup> complex, good agreement is found with the metal in a triplet spin state and the His ligands adopting a hexadentate  $[N_{\alpha},N_{\pi},CO^-][N_{\alpha},N_{\pi},CO]$  conformation. There is also evidence for a small population of zwitterionic  $[N_{\alpha},N_{\pi},CO^-][CO_2^-](N_{\pi}H^+)$ . These observations are inconsistent with DFT approaches, which

predict zwitterionic species as the GS, but MP2 appears to penalize the zwitterionic structure by too much for this complex. Finally, comparison to analogous complexes of Zn and Cd show an inversion in the populated species, as these prefer a zwitterionic form of the neutral His ligand. Differences among the GS structures can be related to steric effects in the complexes with the smaller transition metal dications as compared to that of Ca<sup>2+</sup>, and to the 3d orbital populations.

#### Acknowledgments

Financial support for this work was provided by the National Science Foundation, Grants CHE-1954142. The authors gratefully acknowledge the *Nederlandse Organisatie voor Wetenschappelijk Onderzoek* (NWO) for the support of the FELIX Laboratory. We also appreciate a generous grant of computer time from the Center of High Performance Computing at the University of Utah. MS acknowledges funding from the Deutsche Forschungsgemeinschaft (DFG, grant number SCHA 871/10-1).

#### References

- (1) Ha, N.-C.; Oh, S.-T.; Sung, J. Y.; Cha, K. A.; Lee, M. H.; Oh, B.-H. Supramolecular assembly and acid resistance of Helicobacter pylori urease. *Nature structural biology* **2001**, *8*, 505-509.
- (2) Li, Y.; Zamble, D. B. Nickel homeostasis and nickel regulation: an overview. *Chem. Rev.* **2009,** *109*, 4617-4643.
- (3) Christensen, J.; Kristiansen, J.; Nielsen, N.; Menne, T.; Byrialsen, K. Nickel concentrations in serum and urine of patients with nickel eczema. *Toxicol. Lett.* **1999**, *108*, 185-189.
- (4) Chivers, P. T.; Benanti, E. L.; Heil-Chapdelaine, V.; Iwig, J. S.; Rowe, J. L. Identification of Ni-(L-His) 2 as a substrate for NikABCDE-dependent nickel uptake in Escherichia coli. *Metallomics* **2012**, *4*, 1043-1050.
- (5) Lebrette, H.; Iannello, M.; Fontecilla-Camps, J. C.; Cavazza, C. The binding mode of Ni-(L-His) 2 in NikA revealed by X-ray crystallography. *J. Inorg. Biochem.* **2013**, *121*, 16-18.
- (6) Lebrette, H.; Borezée-Durant, E.; Martin, L.; Richaud, P.; Erba, E. B.; Cavazza, C. Novel insights into nickel import in Staphylococcus aureus: the positive role of free histidine and structural characterization of a new thiazolidine-type nickel chelator. *Metallomics* **2015**, *7*, 613-621.

- (7) Chivers, P. T. Nickel recognition by bacterial importer proteins. *Metallomics* **2015**, *7*, 590-595.
- (8) Peckelsen, K.; Martens, J.; Berden, G.; Oomens, J.; Dunbar, R. C.; Meijer, A. J. H. M.; Schäfer, M. Gas-phase Complexes of Ni<sup>2+</sup> and Ca<sup>2+</sup> with Deprotonated Histidylhistidine (HisHis): A Model Case for Polyhistidyl-metal Binding Motifs. *J. Mol. Spec.* **2017**, *332*, 38-44.
- (9) Polfer, N. C.; Oomens, J.; Dunbar, R. C. IRMPD Spectroscopy of Metal-Ion/Tryptophan Complexes. *Phys. Chem. Chem. Phys.* **2006**, *8*, 2744-2751.
- (10) Drayss, M. K.; Armentrout, P. B.; Oomens, J.; Schäfer, M. IR Spectroscopy of Cationized Aliphatic Amino Acids: Stability of Charge-solvated Structure Increases with Metal Cation Size. *Int. J. Mass Spectrom.* **2010**, *297*, 18–27.
- (11) Bush, M. F.; Oomens, J.; Saykally, R. J.; Williams, E. R. Effects of Alkaline Earth Metal Ion Complexation on Amino Acid Zwitterion Stability: Results from Infrared Action Spectroscopy. *J. Am. Chem. Soc.* **2008**, *130*, 6463-6471.
- (12) Oomens, J.; Polfer, N. C.; Berden, G.; Eyler, J. R. Gas-phase metal ion chelation investigated with IRMPD spectroscopy: A brief review of Robert Dunbar's contributions. *Eur. J. Mass Spectrom.* **2019**, *25*, 86-96.
- (13) Shannon, R. D. Revised Effective Ionic Radii and Systematic Studies of Interatomic Distances in Halides and Chalcogenides. *Acta Cryst.* **1976,** *A32*, 751-767.
- (14) Stevenson, B. C.; Martens, J.; Berden, G.; Oomens, J.; Schäfer, M.; Armentrout, P. B. IRMPD Spectroscopic and Theoretical Structural Investigations of Zinc and Cadmium Dications Bound to Histidine Dimers. *J. Phys. Chem. A* **2020**, *124*, 10266-10276.
- (15) Oepts, D.; van der Meer, A. F. G.; van Amersfoort, P. W. The Free-Electron-Laser User Facility FELIX. *Infrared Phys. Technol.* **1995**, *36*, 297-308.
- (16) Martens, J.; Berden, G.; Gebhardt, C. R.; Oomens, J. Infrared ion spectroscopy in a modified quadrupole ion trap mass spectrometer at the FELIX free electron laser laboratory. *Rev. Sci. Instrum.* **2016**, *87*, 103108.
- (17) Ke, S. Y.; Wang, C. C.; Lee, G. H.; Chuang, Y. C.; Lu, K. L. Highly Thermal-Stable Supramolecular Assembly of a Hydrogen-Bonded Mononuclear Nickel (II) Histidine Compound. *J. Chinese Chem. Soc.* **2013**, *60*, 807-812.
- (18) Berden, G.; Derksen, M.; Houthuijs, K. J.; Martens, J.; Oomens, J. An Automatic Variable Laser Attenuator for IRMPD Spectroscopy and Analysis of Power-dependence in Fragmentation Spectra. *Int. J. Mass Spectrom.* **2019**, *443*, 1-8.
- (19) Lemaire, J.; Boissel, P.; Heninger, M.; Mauclaire, G.; Bellec, G.; Mestdagh, H.; Le Caer, S.; Ortega, J.; Glotin, F.; Maître, P. Gas Phase Infrared Spectroscopy of Selectively Prepared Ions. *Phys. Rev. Lett.* **2002**, *89*, 273002.
- (20) Frisch, M. J.; Trucks, G. W.; Schlegel, H. B.; Scuseria, G. E.; Robb, M. A.; Cheeseman, J. R.; Scalmani, G.; Barone, V.; Petersson, G. A.; Nakatsuji, H., et al. *Gaussian 16, Revision A.03*, Gaussian, Inc.: Wallingford CT, 2016.
- (21) Polfer, N. C. Infrared Multiple Photon Dissociation Spectroscopy of Trapped Ions. *Chem. Soc. Rev.* **2011**, *40*, 2211–2221.
- (22) Hofstetter, T. E.; Howder, C.; Berden, G.; Oomens, J.; Armentrout, P. B. Structural Elucidation of Biological and Toxicological Complexes: Investigation of Monomeric and Dimeric Complexes of Histidine with Multiply Charged Transition Metal (Zn and Cd) Cations using IR Action Spectroscopy. *J. Phys. Chem. B* **2011**, *115*, 12648-12661.
- (23) Coates, R. A.; Boles, G. C.; McNary, C. P.; Berden, G.; Oomens, J.; Armentrout, P. B. Zn<sup>2+</sup> and Cd<sup>2+</sup> Cationized Serine Complexes: Infrared Multiple Photon Dissociation

- Spectroscopy and Density Functional Theory Investigations. *Phys. Chem. Chem. Phys.* **2016**, *18*, 22434 22445.
- (24) Coates, R. A.; McNary, C. P.; Boles, G. C.; Berden, G.; Oomens, J.; Armentrout, P. B. Structural Characterization of Gas-Phase Cysteine and Cysteine Methyl Ester Complexes with Zinc and Cadmium Dications by Infrared Multiple Photon Dissociation Spectroscopy. *Phys. Chem. Chem. Phys.* **2015**, *17*, 25799-25808.
- (25) Boles, G. C.; Coates, R. A.; Berden, G.; Oomens, J.; Armentrout, P. B. Experimental and Theoretical Investigations of Infrared Multiple Photon Dissociation Spectra of Glutamine Complexes with Zn<sup>2+</sup> and Cd<sup>2+</sup>. *J. Phys. Chem. B* **2015**, *119*, 11607–11617.
- (26) Chalifoux, A. M.; Boles, G. C.; Berden, G.; Oomens, J.; Armentrout, P. B. Experimental and Theoretical Investigations of Infrared Multiple Photon Dissociation Spectra of Arginine Complexes with Zn<sup>2+</sup> and Cd<sup>2+</sup>. *Phys. Chem. Chem. Phys.* **2018**, *20*, 20712-20725.
- (27) Owen, C. J.; Boles, G. C.; Berden, G.; Oomens, J.; Armentrout, P. B. Experimental and Theoretical Investigations of Infrared Multiple Photon Dissociation Spectra of Lysine Complexes with Zn<sup>2+</sup> and Cd<sup>2+</sup>. *Eur. J. Mass Spectrom.* **2019**, *25*, 97-111.
- (28) Boles, G. C.; Owen, C. J.; Berden, G.; Oomens, J.; Armentrout, P. B. Experimental and Theoretical Investigations of Infrared Multiple Photon Dissociation Spectra of Glutamic Acid Complexes with Zn<sup>2+</sup> and Cd<sup>2+</sup>. *Phys. Chem. Chem. Phys.* **2017**, *19*, 12394 12406.
- (29) Boles, G. C.; Hightower, R. L.; Coates, R. A.; McNary, C. P.; Berden, G.; Oomens, J.; Armentrout, P. B. Experimental and Theoretical Investigations of Infrared Multiple Photon Dissociation Spectra of Aspartic Acid Complexes with Zn<sup>2+</sup> and Cd<sup>2+</sup>. *J. Phys. Chem. B* **2018**, *122*, 3836-3853.
- (30) Kesharwani, M. K.; Brauer, B.; Martin, J. M. L. Frequency and Zero-Point Vibrational Energy Scale Factors for Double-Hybrid Density Functionals (and Other Selected Methods): Can Anharmonic Force Fields Be Avoided? *J. Phys. Chem. A* **2015**, *119*, 1701-1714.
- (31) Grimme, S.; Ehrlich, S.; Goerigk, L. Effect of the Damping Function in Dispersion Corrected Density Functional Theory. *J. Comput. Chem.* **2011**, *32*, 1456-1465.
- (32) Grimme, S.; Antony, J.; Ehrlich, S.; Krieg, H. A Consistent and Accurate Ab Initio Parametrization of Density Functional Dispersion Correction (DFT-D) for the 94 Elements H-Pu. *J. Chem. Phys.* **2010**, *132*, 154104-154119.
- (33) Valle, J. J.; Eyler, J. R.; Oomens, J.; Moore, D. T.; van der Meer, A. F. G.; von Heldon, G.; Meijer, G.; Hendrickson, C. L.; Marshall, A. G.; Blakney, G. T. Free Electron Laser-Fourier Transform Ion Cyclotron Resonance Mass Spectrometry Facility for Obtaining Infrared Multiphoton Dissociation Spectra of Gaseous Ions. *Rev. Sci. Instrum.* **2005**, *76*, 023103.
- (34) Polfer, N. C.; Oomens, J.; Moore, D. T.; von Helden, G.; Meijer, G.; Dunbar, R. C. Infrared Spectroscopy of Phenylalanine Ag(I) and Zn(II) Complexes in the Gas Phase. *J. Am. Chem. Soc.* **2006**, *128*, 517-525.
- (35) Polfer, N. C.; Oomens, J. Reaction products in mass spectrometry elucidated with infrared spectroscopy. *Phys. Chem. Chem. Phys.* **2007**, *9*, 3804-3817.
- (36) Munshi, M. U.; Berden, G.; Martens, J.; Oomens, J. Gas-phase vibrational spectroscopy of triphenylamine: the effect of charge on structure and spectra. *Phys. Chem. Chem. Phys.* **2017**, *19*, 19881-19889.
- (37) Boles, G. C.; Coates, R. A.; Berden, G.; Oomens, J.; Armentrout, P. B. Experimental and Theoretical Investigations of Infrared Multiple Photon Dissociation Spectra of Asparagine Complexes with Zn<sup>2+</sup> and Cd<sup>2+</sup> and Their Deamidation Processes. *J. Phys. Chem. B* **2016**, *120*, 12486-12500.

- (38) Armentrout, P. B.; Rodgers, M. T.; Oomens, J.; Steill, J. D. Infrared Multiphoton Dissociation Spectroscopy of Cationized Serine: Effects of Alkali-Metal Cation Size on Gas-Phase Conformation. *J. Phys. Chem. A* **2008**, *112*, 2248-2257.
- (39) Rodgers, M. T.; Armentrout, P. B.; Oomens, J.; Steill, J. D. Infrared Multiphoton Dissociation Spectroscopy of Cationized Threonine: Effects of Alkali-Metal Cation Size on Gas-Phase Conformation. *J. Phys. Chem. A* **2008**, *112*, 2258-2267.
- (40) Citir, M.; Hinton, C. S.; Oomens, J.; Steill, J. D.; Armentrout, P. B. Infrared Multiple Photon Dissociation Spectroscopy of Cationized Histidine: Effects of Metal Cation Size on Gas-Phase Conformation. *J. Phys. Chem. A* **2012**, *116*, 1532-1541.
- (41) Citir, M.; Stennett, E. M. S.; Oomens, J.; Steill, J. D.; Rodgers, M. T.; Armentrout, P. B. Infrared Multiple Photon Dissociation Spectroscopy of Cationized Cysteine: Effects of Metal Cation Size on Gas-Phase Conformation. *Int. J. Mass Spectrom.* **2010**, *297*, 9-17.
- (42) Fraser, K.; Harding, M. M. The crystal and molecular structure of bis (histidino) nickel (II) monohydrate. *J. Chem. Soc. A: Inorg., Phys., Theor.* **1967**, 415-420.

**Table 1.** Relative Enthalpies at 0 K (Gibbs Energies at 298 K) in kJ/mol of Low-Lying Ca(His-H)(His)<sup>+</sup> Complexes<sup>a</sup>

Structure	B3LYP	B3LYP-GD3BJ <sup>b</sup>	B3P86	MP2(full)
	4.2 (0.0)	4.4 (0.0)	4.2 (0.0)	0.0 (0.0)
$[N_{\alpha},\!N_{\pi},\!CO^{-}][CO_{2}^{-}](N_{\pi}H^{+})$	0.0 (0.3)	0.0 (1.3)	0.0 (0.4)	8.6 (13.1)
$[N_\pi,\!CO_2^-][N_\alpha,\!N_\pi,\!CO]gtgg$	5.5 (3.5)	7.0 (5.5)	6.5 (4.6)	2.5 (4.8)
$[N_\alpha,\!N_\pi,\!CO^-][N_\alpha,\!N_\pi,\!CO](1)$	13.0 (11.6)	6.8 (5.3)	14.5 (13.2)	7.5 (10.3)
$[N_\pi,\!CO_2^-][N_\alpha,\!N_\pi,\!CO]g\_tgg(2)$	13.5 (8.9)	13.3 (10.8)	15.1 (15.0)	10.1 (9.7)
$[N_\alpha,\!N_\pi,\!CO^-][CO_2^-](N_\alpha H^+)$	15.7 (20.1)	5.5 (12.0)	9.1 (13.5)	3.2 (11.7)
$[N_\alpha,\!N_\pi,\!CO^-][N_\alpha,\!N_\pi,\!CO](2)$	21.5 (19.6)	15.3 (12.3)	22.9 (21.0)	15.4 (17.7)
$[N_\alpha,\!N_\pi,\!CO^-][N_\alpha,\!CO](N_\pi H^+)$	38.8 (39.7)	25.8 (28.9)	36.6 (37.6)	38.8 (43.9)
$[N_\alpha,\!N_\pi,\!CO^-][N_\alpha,\!N_\pi]$	48.7 (41.3)	50.7 (36.7)	52.0 (44.7)	59.0 (55.8)

<sup>a</sup>Calculated at the level of theory specified using a 6-311+G(2d,2p) basis set and B3LYP/6-311+G(d,p) geometries.  $^b$ B3LYP-GD3BJ/6-311+G(2d,2p)//B3LYP-GD3BJ/6-311+G(d,p) results.

**Table 2.** Metal-Coordination Bond Distances (Å) for Low-lying M(His-H)(His)<sup>+</sup> Complexes<sup>a</sup>

Charachara	(His-H) <sup>-</sup>			His		
Structure	$M$ - $N_{\alpha}^{\ b}$	$M$ - $N_{\pi}$	М-О	$M$ - $N_{a}^{b}$	$M$ - $N_{\pi}$	М-О
$Ca^{2+}[N_{\pi},CO_{2}^{-}][N_{\alpha},N_{\pi},CO]g.tgg(1)$	2.321 <sup>c</sup>	2.530	2.321	2.598	2.478	2.476
$Ca^{2+}[N_{\alpha},N_{\pi},CO^{-}][CO_{2}^{-}](N_{\pi}H^{+})$	2.542	2.457	2.257	2.355 <sup>c</sup>		2.328
$Ca^{2^+}\left[N_\pi,CO_2^-\right]\!\left[N_\alpha,\!N_\pi,\!CO\right]\!gtgg$	2.345 <sup>c</sup>	2.523	2.299	2.591	2.474	2.488
$Ca^{2^{+}}[N_{\alpha},N_{\pi},CO^{-}][N_{\alpha},N_{\pi},CO](1)$	2.509	2.473	2.214	2.637	2.487	2.500
$Ca^{2+}  [N_\pi, CO_2^-] [N_\alpha, N_\pi, CO] g.tgg(2)$	2.331 <sup>c</sup>	2.547	2.331	2.645	2.487	2.446
$Ca^{2^{+}}[N_{\alpha},\!N_{\pi},\!CO^{-}][CO_{2}^{-}](N_{\alpha}H^{+})$	2.538	2.442	2.194	2.423 <sup>c</sup>		2.422
$Ca^{2+} [N_{\alpha}, N_{\pi}, CO^{-}][N_{\alpha}, N_{\pi}, CO](2)$	2.497	2.479	2.212	2.528	2.567	2.479
$Ca^{2^+}\left[N_\alpha,\!N_\pi,\!CO^-\right]\!\left[N_\alpha,CO\right]\!\left(N_\pi H^+\right)$	2.570	2.435	2.282	2.569		2.198
$Ca^{2+}$ [N <sub><math>\alpha</math></sub> ,N <sub><math>\pi</math></sub> ,CO <sup>-</sup> ][N <sub><math>\alpha</math></sub> ,N <sub><math>\pi</math></sub> ]	2.498	2.451	2.195	2.609	2.421	
$Ni^{2^+}\left[N_\alpha,\!N_\pi,\!CO^-\right]\!\left[N_\alpha,\!N_\pi,\!CO\right]$	2.108	2.093	1.996	2.151	2.131	2.314
$Ni^{2^+}\left[N_\alpha,\!N_\pi,\!CO^-\right]\!\left[N_\alpha,N_\pi\right]$	2.088	2.077	1.996	2.187	2.066	$2.453^{d}$
$Ni^{2^+}[N_\alpha,\!N_\pi,\!CO^-][CO_2^-](N_\pi H^+)$	2.088	2.028	1.998	2.094 <sup>c</sup>		2.079
$Ni^{2^+}  [N_\alpha,\! N_\pi,\! CO^-] [N_\alpha,\! CO^-] (N_\pi H^+)$	2.137	2.056	2.017	2.128		1.967
$Ni^{2+}$ [N <sub><math>\pi</math></sub> ,CO <sub>2</sub> <sup>-</sup> ][N <sub><math>\alpha</math></sub> ,N <sub><math>\pi</math></sub> ,CO]	2.162 <sup>c</sup>	2.125	2.063	2.105	2.076	2.287
$Ni^{2^+}  [N_\alpha,\!N_\pi,\!CO^-] [CO_2^-] (N_\alpha H^+)$	2.073	2.019	1.957	2.179 <sup>c</sup>		2.127
$Ni^{2^+}  [N_\alpha,\!CO^-] [N_\alpha,\!N_\pi] ttgt^1$	1.935		1.833	1.973	1.926	
$Ni^{2^+}  [N_\alpha,\!CO^-][N_\alpha,\!N_\pi] ttgg^1$	1.928		1.830	1.967	1.921	
$Ni^{2^{+}}\left[N_{\alpha},N_{\pi}\right]\left[N_{\alpha},CO^{-}\right]\left(N_{\pi}H^{+}\right)^{1}$	1.962	1.905	3.071	1.942		1.846

<sup>&</sup>lt;sup>a</sup> Distances shown from structures calculated at B3LYP/ 6-311+G(d,p) level. <sup>b</sup> Except as noted.

<sup>&</sup>lt;sup>c</sup> M-O. <sup>d</sup>Distance from B3LYP-GD3BJ/6-311+G(d,p) optimized geometry.

**Table 3.** Relative Enthalpies at 0 K (Gibbs Energies at 298 K) in kJ/mol of Low-Lying Ni(His-H)(His)<sup>+</sup> Complexes<sup>a</sup>

Structure	B3LYP	B3LYP-GD3BJ <sup>b</sup>	B3P86	MP2(full)
$\boxed{ [N_{\alpha},N_{\pi},CO^{-}][N_{\alpha},N_{\pi},CO] }$	6.1 (8.8)	0.3 (0.5)	0.0 (2.3)	0.0 (0.0)
$[N_\alpha,\!N_\pi,\!CO^-][N_\alpha,\!N_\pi]$	7.2 (8.2)	$0.0  (0.0)^c$	3.9 (4.3)	12.0 (10.2)
$[N_{\alpha},\!N_{\pi},\!CO^{-}][CO_{2}^{-}](N_{\pi}H^{+})$	0.0 (0.0)	12.4 (9.2)	0.5 (0.0)	29.2 (26.5)
$[N_\alpha,\!N_\pi,\!CO^-][N_\alpha,\!CO^-](N_\pi H^+)$	12.4 (13.7)	11.1 (9.4)	9.9 (10.6)	31.2 (29.8)
$[N_\pi,CO_2^-][N_\alpha,N_\pi,CO]$	25.3 (26.8)	26.1 (25.1)	20.0 (21.0)	26.5 (25.2)
$[N_\alpha,\!N_\pi,\!CO^-][CO_2^-](N_\alpha H^+)$	25.2 (25.1)	26.1 (26.0)	21.4 (20.8)	39.4 (36.5)
$[N_\alpha,\!CO^-][N_\alpha,\!N_\pi]ttgt^1$	22.7 (21.4)	35.0 (30.4)	17.4 (15.6)	75.7 (71.6)
$[N_\alpha,\!CO^-][N_\alpha,\!N_\pi]ttgg^1$	24.9 (24.7)	35.1 (31.9)	18.8 (18.0)	72.1 (69.1)
$[N_\alpha,\!N_\pi][N_\alpha,\!CO^-](N_\pi H^+)^1$	25.6 (35.7)	16.2 (24.3)	14.0 (23.6)	56.4 (63.8)

<sup>&</sup>lt;sup>a</sup>Calculated at the level of theory indicated using a 6-311+G(2d,2p) basis set and B3LYP/6-311+G(d,p) geometries. All species have triplet spin except as indicated by <sup>1</sup> for singlet spin. <sup>b</sup> B3LYP-GD3BJ/6-311+G(2d,2p)//B3LYP-GD3BJ/6-311+G(d,p) results. <sup>c</sup> Optimized structure converged to [Nα,Nπ,CO<sup>-</sup>][Nα,Nπ,CO], where the lower-energy structure has the imidazole rings pointing in opposite directions, and the higher-energy structure has them pointing in the same direction.

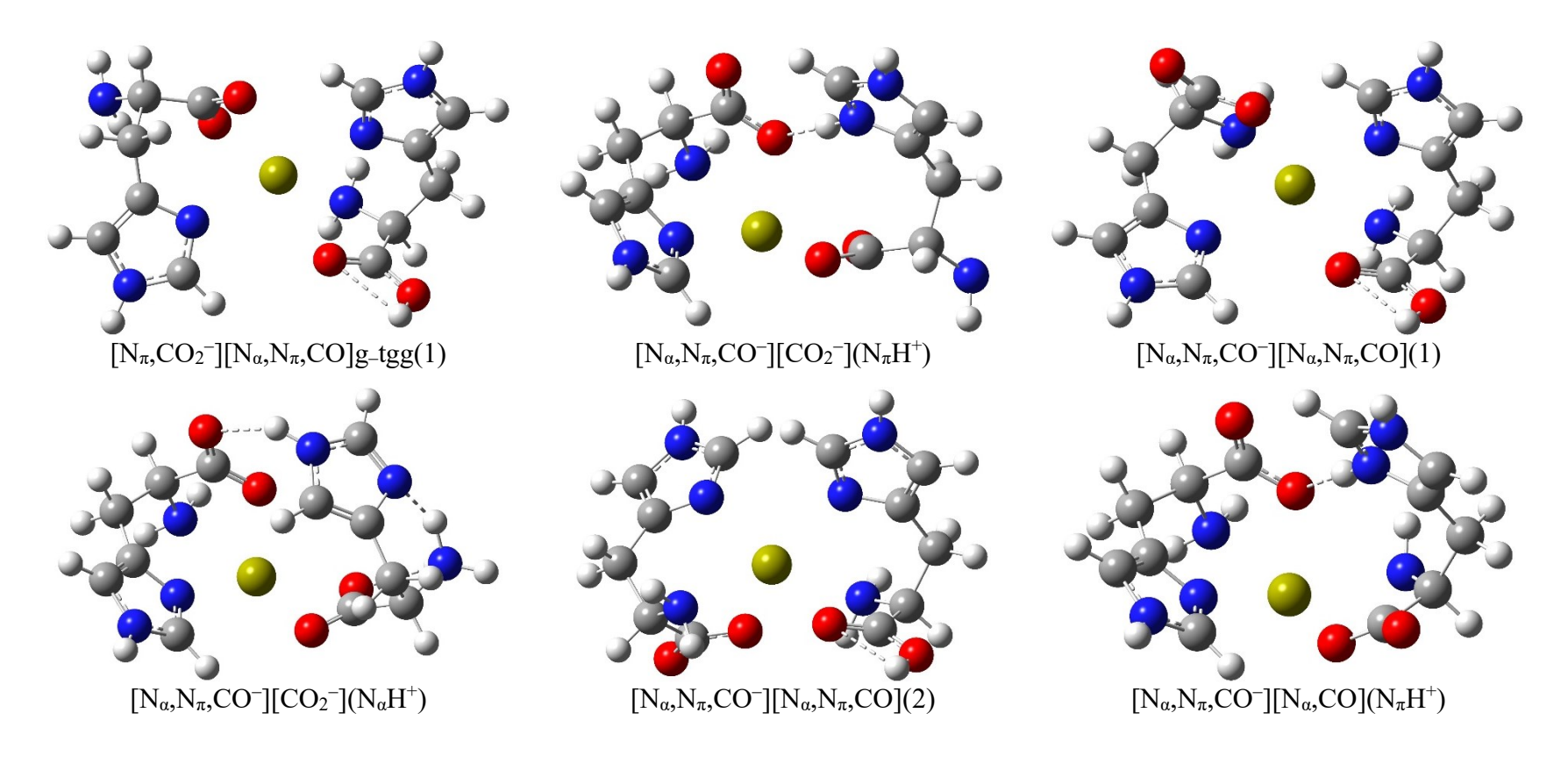


**Figure 1.** Structures of select Ca(His-H)(His)<sup>+</sup> conformers calculated at the B3LYP/6-311+G(d,p) level of theory. Dashed lines indicate hydrogen bonds. (Red—oxygen, grey—carbon, white—hydrogen, blue—nitrogen, dark yellow—calcium).

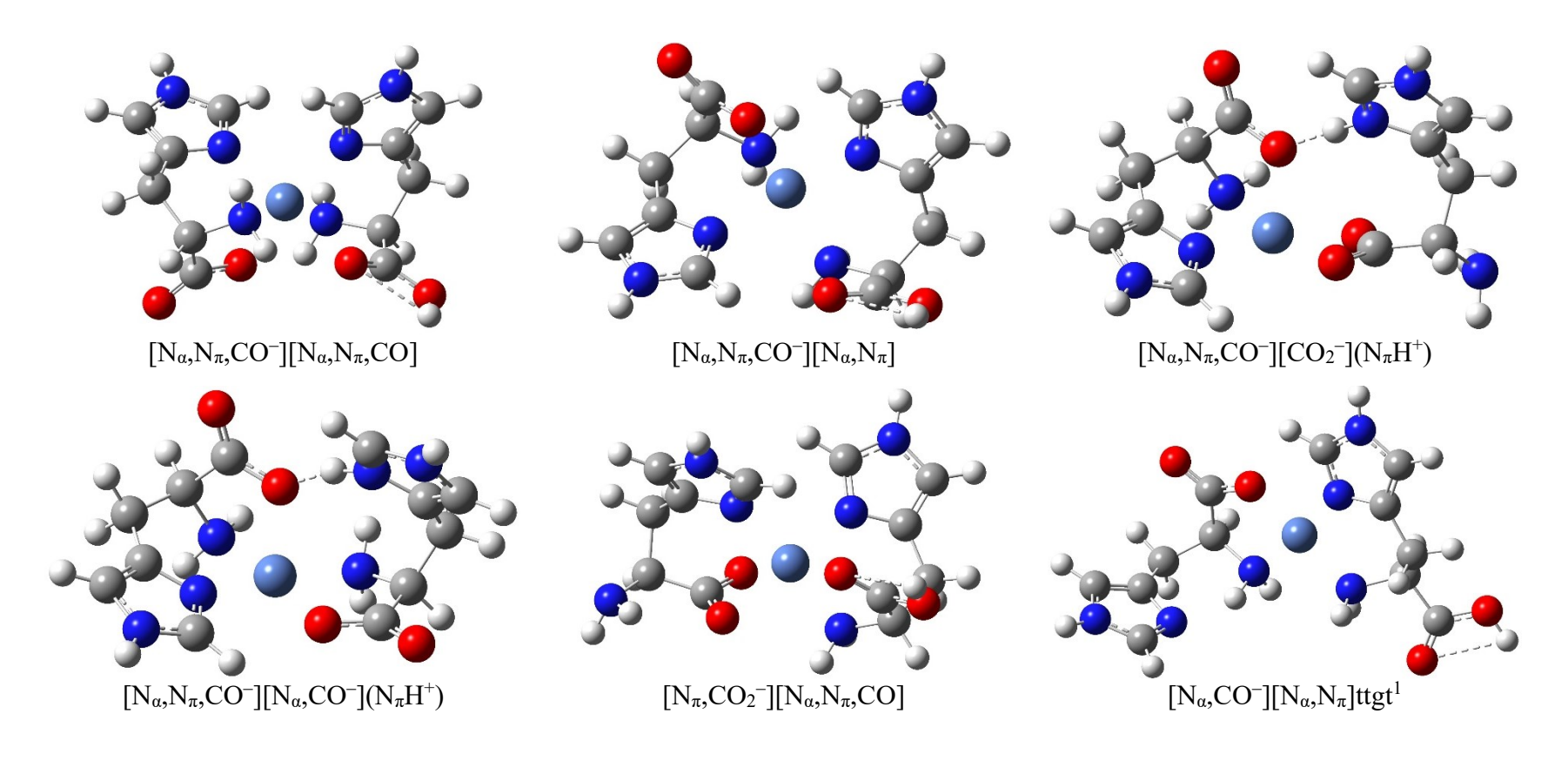


**Figure 2.** Structures of select Ni(His-H)(His)<sup>+</sup> conformers calculated at the B3LYP/6-311+G(d,p) level of theory. Dashed lines indicate hydrogen bonds. (Red—oxygen, grey—carbon, white—hydrogen, blue—nitrogen, steel blue—nickel).

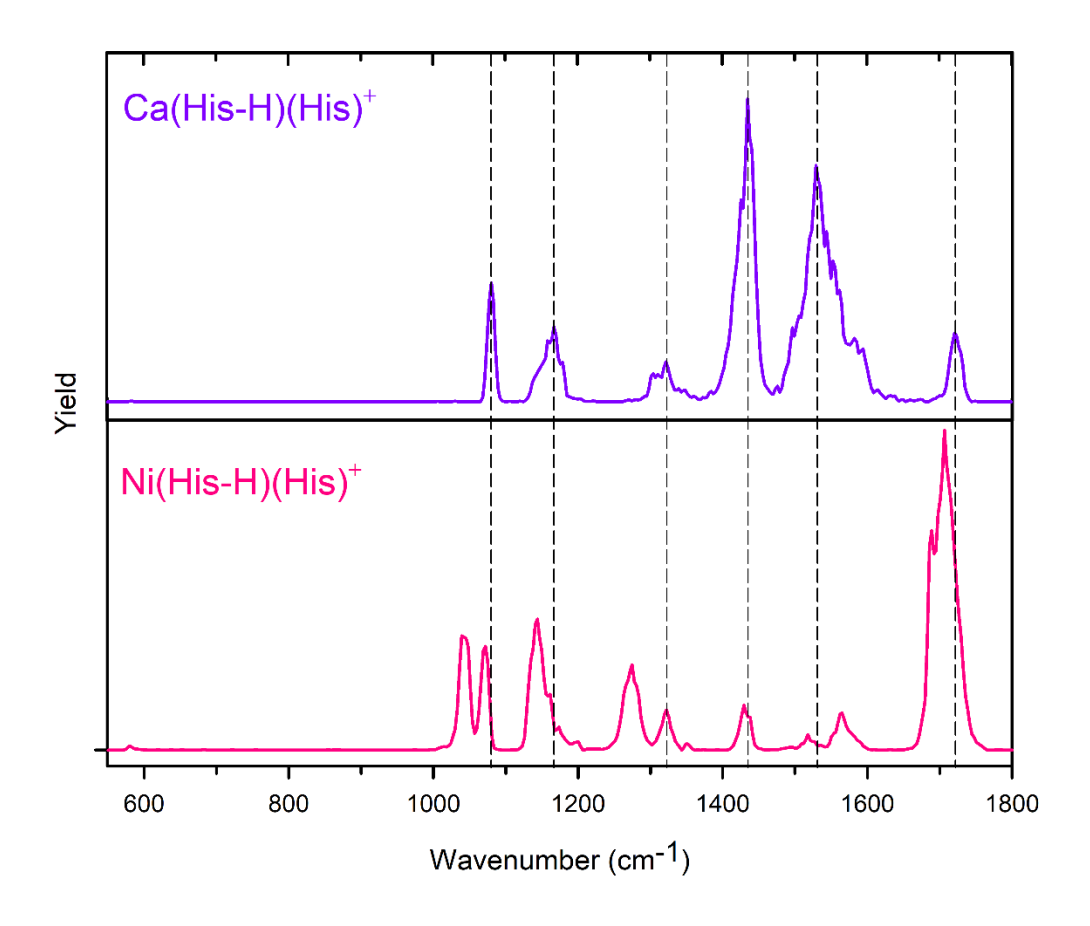


**Figure 3.** Comparison of the Ca(His-H)(His)<sup>+</sup> and Ni(His-H)(His)<sup>+</sup> IRMPD action spectra. Vertical dashed lines mark the peaks in the Ca spectrum and allow facile comparison of shifts in the Ni system.

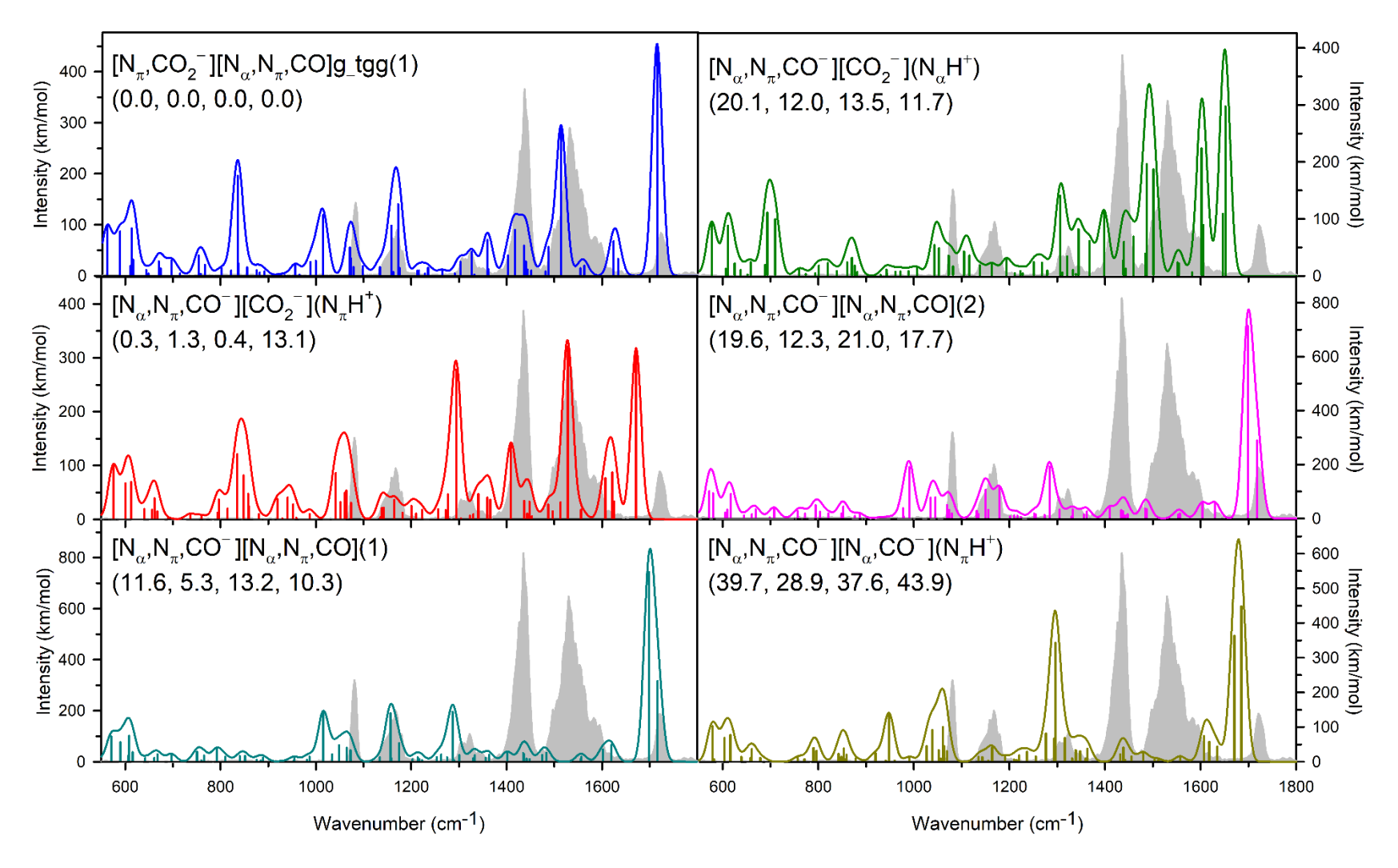


**Figure 4.** Comparison of the Ca(His-H)(His)<sup>+</sup> experimental IRMPD action spectrum, shown here as the light grey shadow, with IR spectra calculated at the B3LYP/6-311+G(d,p) level of theory for low-lying conformers. Relative 298 K Gibbs energies (kJ/mol) are given at the B3LYP, B3LYP-GD3BJ, B3P86, and MP2 levels, respectively.

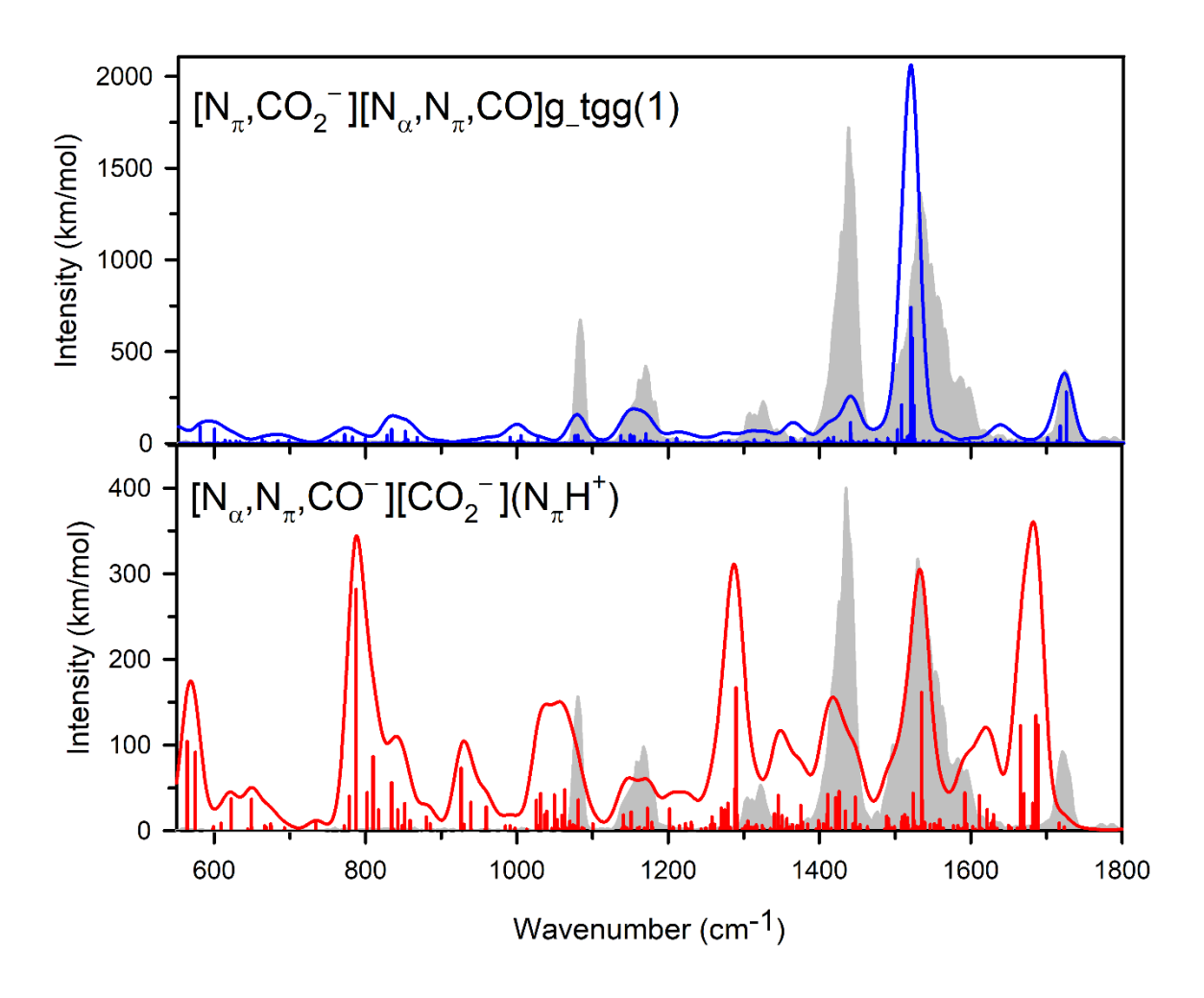


**Figure 5.** Comparison of the Ca(His-H)(His)<sup>+</sup> experimental IRMPD spectrum and the anharmonic spectra calculated for the two lowest-lying conformers calculated at the B3LYP/6-311+G(d,p) level with the keyword "freq=anharmonic".

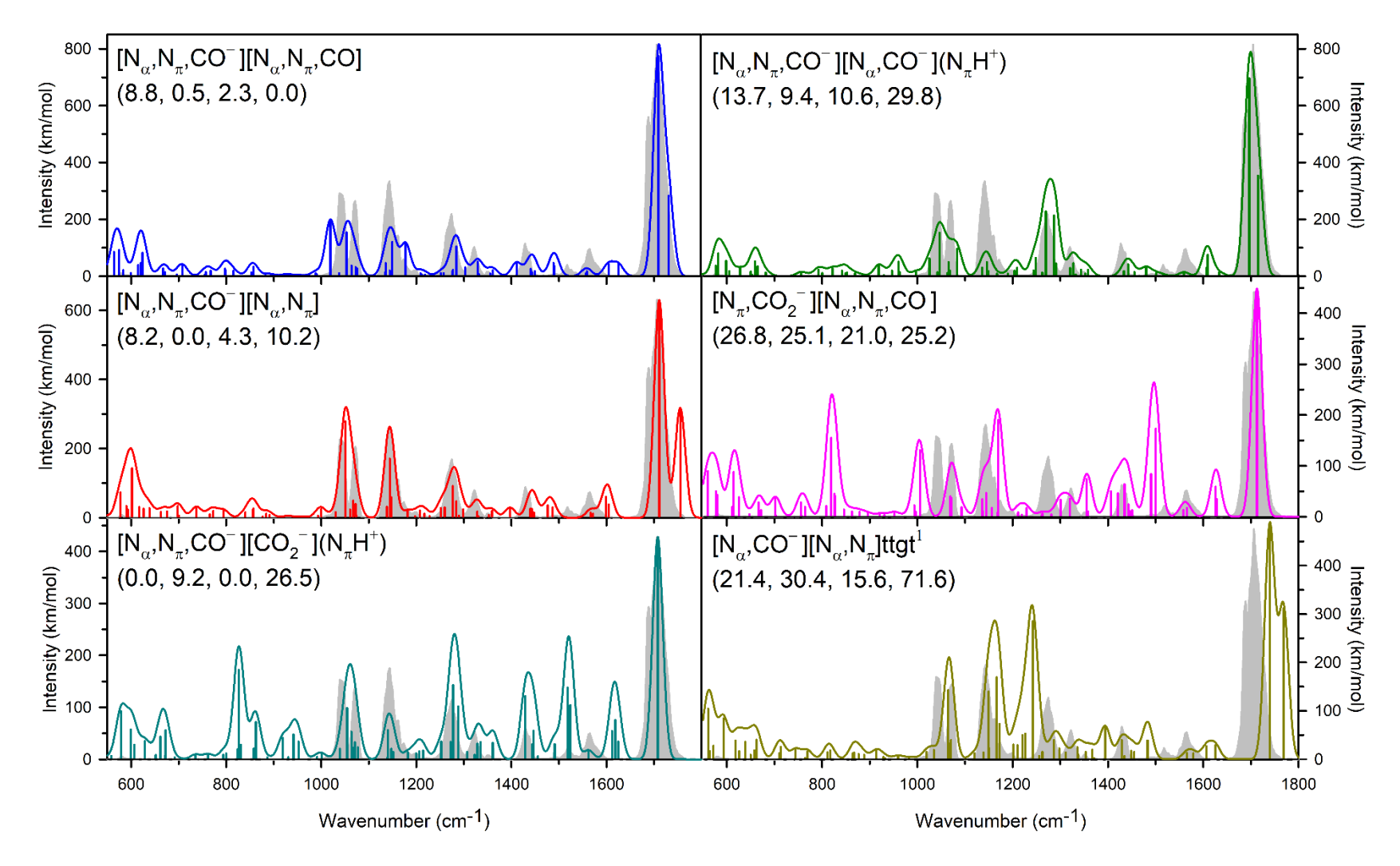


**Figure 6.** Comparison of the Ni(His-H)(His)<sup>+</sup> experimental IRMPD action spectrum collected on the QIT instrument, shown here as the light grey shadow, with IR spectra calculated at the B3LYP/6-311+G(d,p) level of theory for low-lying conformers. Relative 298 K Gibbs energies (kJ/mol) are given at the B3LYP, B3LYP-GD3BJ, B3P86, and MP2 levels, respectively.